RESEARCH ARTICLE

Clinopyroxene growth rates at high pressure: constraints on magma recharge of the deep reservoir of the Campi Flegrei Volcanic District (south Italy)

B. Bonechi[1] ⬤ · C. Perinelli[1] · M. Gaeta[1]

Abstract

Clinopyroxene growth rates were experimentally determined in a K-basaltic rock from Campi Flegrei Volcanic District (south Italy). The primary objective was to provide constraints on the clinopyroxene crystallization kinetics at high pressure: we carried out a series of experiments at 0.8 GPa, 1030–1250 °C, $1 \le H_2O \le 4$ wt.%, with durations of 0.25, 3, 6 and 9 h. Overall, growth rate reaches a maximum value in the shortest experiments ($\sim 3 \cdot 10^{-7}$ cm·s^{-1}), decreasing to $\sim 1 \cdot 10^{-8}$ cm·s^{-1} in the longest duration runs. Temperature and water content do not seem to significantly affect the growth rate. Moreover, partition coefficients based on the crystal-liquid exchange show that mineral chemistry progressively approaches equilibrium with increasing run duration. Furthermore, to estimate the magma recharge of the deep reservoirs, we combined the determined growth rates with data from thermobarometry and from crystal size distribution analyses of clinopyroxenes in the most primitive scoria clasts of the Campi Flegrei Volcanic District (CFVD). We obtained a minimum residence time of ~ 5 months for the larger clinopyroxene population, and an ascent velocity of $\sim 0.5 \cdot 10^{-4}$ m·s^{-1} for the CFVD K-basaltic magma. The smaller clinopyroxene phenocrysts and microlite populations, however, suggest that the late stage of Procida magma crystallization took place in disequilibrium conditions.

Introduction

The kinetics of crystal nucleation and growth are fundamental for the interpretation of rock textures in terms of thermal history of a magma during its ascent to the surface and to constrain time-scales of magmatic processes. Crystallization kinetics has been investigated in lunar and terrestrial basalts (Dowty et al. 1974; Lofgren 1974, 1983; Grove and Walker 1977; Grove and Raudsepp 1978; Walker et al. 1978; Lesher et al. 1999) and in silicic hydrous systems (Lofgren 1980; Kirkpatrick et al. 1981;

Hammer and Rutherford 2002; Hammer 2006; Zieg and Lofgren 2006; Pupier et al. 2008). However, there are relatively few investigations of alkaline compositions (e.g. Conte et al. 2006; Agostini et al. 2013; Arzilli et al. 2015).

Clinopyroxene (Cpx) is a common phenocryst in basaltic systems and, due to its wide crystallization range, it may contain the most complete record of evolutionary history of a magma. To date, experimental studies of Cpx crystallization kinetics (e.g. crystal growth rate) in primitive alkaline compositions are few and limited to low pressure conditions (≤ 0.5 GPa; e.g. Orlando et al. 2008; Arzilli and Carroll 2013; Pontesilli et al. 2019). To constrain clinopyroxene crystallization kinetics at high pressure, we experimentally investigated the growth rate of clinopyroxene in an alkaline basalt (APR16 sample; Bonechi et al. 2017) representative of the least-evolved rocks of the whole Campi Flegrei Volcanic District (CFVD). Both anhydrous and hydrous experiments were conducted at a pressure of ~ 0.8 GPa that is representative of the crustal-mantle boundary (~ 25 km of depth; Di Stefano et al. 2011) in the Phlegraean area, and the location of a possible crystallization zone, hypothesized on the basis of melt inclusion studies (Mormone et al. 2011; Moretti et al. 2013),

✉ B. Bonechi
barbara.bonechi@uniroma1.it

1   Dipartimento di Scienze della Terra, Sapienza Università di Roma, P.le Aldo Moro 5, 00185 Rome, Italy

seismic data (Di Stefano et al. 1999; Piochi et al. 2005a, b; Chiarabba et al. 2008) and gravimetric and petrological modelling (Fedi et al. 2018). Moreover, Perinelli et al. (2019) demonstrated that early magmatic storage and crystallization at high pressure (i.e. at the local crust base) contributed to the differentiation of primitive magmas of the Campania Province. For these reasons, the experimental data on high-pressure clinopyroxene growth kinetic will be useful for constraining timescales of magmatic processes in this area. In particular, the estimation of the magma ascent rate in the CFVD is of paramount significance in terms of volcanic hazard. Indeed, deep-level ascent rates may be the key to understand the triggering mechanisms of volcanic eruptions, and are essential for understanding the rates at which magmas are supplied to volcanic complexes (Armienti et al. 2013; Perinelli et al. 2018). Thus, to investigate the CFVD magmas transport at Moho-lower crust depth and provide an estimate of magma recharge of the deep reservoirs, we assessed the cooling rate and the deep-level ascent rates of K-basaltic magmas by combining the clinopyroxene growth rate determined by high-pressure crystallization experiments with data from crystal size distribution analyses and thermobarometry of clinopyroxenes occurring in the most primitive scoria clasts of the CFVD.

Experimental and analytical techniques

Starting material

The starting material used in this work is an anhydrous glass (APR16GL; Table 1) prepared by melting the APR16 natural powder in a gas-mixing furnace at 1400 °C and atmospheric

Table 1 Composition (wt.%) of APR16 rock sample, APR16GL starting material, SCE and SOG rock samples

Sample	APR16	APR16GL	SCE	SOG
SiO_2	48.89	49.30	47.62	47.78
TiO_2	1.23	1.33	1.23	1.23
Al_2O_3	15.65	15.31	15.33	15.43
FeO_{tot}	8.08	7.79	8.19	8.24
MnO	0.14	0.14	0.14	0.15
MgO	8.89	9.31	9.78	9.75
CaO	11.64	12.02	11.89	11.59
Na_2O	2.88	2.86	2.69	2.83
K_2O	1.52	1.60	1.58	1.67
P_2O_5	0.31	0.33	0.29	0.29
Sum	99.99	99.23	99.65	99.88
L.O.I.	0.61	nd	0.26	0.28
Mg#[1]	0.66	0.68	0.68	0.68

[1] [$MgO/(MgO + FeO_{tot})$] molar, assuming all Fe^{2+} and Fe^{3+} as FeO_{tot}. Chemical composition of APR16 is from D'Antonio et al. (1999); APR16GL composition is from Perinelli et al. (2019); SCE from Granati (2016). SOG from this study

pressure for 15 min to reduce all Fe^{3+} to Fe^{2+} using a CO/CO_2 gas mixture at the Bayerisches Geoinstitut (Bayreuth, Germany). The starting material did not contain crystalline phases, as analysed by both microprobe and image analyses. The APR16 sample (Table 1) is a primitive alkaline basalt found as scoria clast in the deposits of the Solchiaro hydromagmatic centre located in Procida island (Campi Flegrei, Italy). It is characterized by 12 vol.% of forsteritic olivine and diopsidic clinopyroxene phenocrysts in a groundmass of olivine, clinopyroxene, plagioclase, Ti-magnetite, alkali feldspar and glass (D'Antonio et al. 1999; De Astis et al. 2004).

Experimental technique

Experiments were performed, at the isobaric pressure of 0.8 GPa, as function of temperature, water content and time by using the ½ inch end loaded piston cylinder apparatus at the HP-HT Laboratory of the Earth Sciences Department (Sapienza University, Rome, Italy). The assembly consists of an outer CaF_2 cell, graphite furnace and MgO crushable spacers. Firstly, the APR16GL glass was crushed and ground in an agate mortar under acetone to a grain size ≤ 10 μm. Then this glassy powder (40–50 mg) was dried at 110 °C for at least 2 h to remove the moisture before being loaded and pressed into $Au_{75}Pd_{25}$ capsules, along with distilled water for hydrous experiments, and then welded. For each experiment, the capsule was placed in the MgO crushable spacers and surrounded by powder of alumina (for no water added experiments) or pyrophyllite (for water added ones). Temperature was measured using a type D W_3Re_{97}-$W_{25}Re_{75}$ thermocouple and maintained with an uncertainty of ± 5 °C. The experimental assembly was first pressurized to the target pressure by a piston-out procedure (Johannes et al. 1971; Presnall et al. 1978) that applies an overpressure of ~ 10% of the run pressure and then gradually increases the temperature to the working temperature, while correcting for pressure drops due to stress relaxation within the assembly during heating. The heating rate was imposed at 150 °C/min. The sample was maintained at the pressure and temperature for a given duration (nominal duration), and then quenched by turning off the power. The temperature dropped to below 500 °C within < 5 s (average cooling rate of 150 °C/s). All the runs were self-buffered; we estimated fO_2 through the equation of Kress and Carmichael (1991) using the liquid Fe^{3+}/Fe_{tot} mole ratios from K_D Fe-Mg ol/liq calculated following Toplis (2005). This procedure yielded fO_2 values of $\Delta NNO + 0.12$ to $+ 2$, in agreement with those estimated for similar furnace assemblages (Conte et al. 2009; Weaver et al. 2013). We performed a total of 24 experiments, whose experimental conditions are reported in Table 2. The experiments were divided into three series based on the amount of water added to the starting material. All series were run at a constant pressure and at four different dwell times (0.25, 3, 6 and 9 h). Experiments of *Series 1* (i.e. APR16-C1) were run at anhydrous conditions (no water added to the starting

Table 2 Experimental run conditions, calculated water contents, phase assemblages and proportions in run products

Run #	T (°C)	TCpx$_L$ (°C)	ΔT_{eff} (°C)	Time (h)	H_2O_i (wt%)	Phases	H_2O_f (wt%)	Σr^2	% $\Delta Fe^{§}$
Series 1									
Subseries C1A									
APR16-C1Aa	1250	1295	45	0.25	NWA	Gl(97) + Cpx(3)	1.61	1.75	−7
APR16-C1Ab	1250	1295	45	3	NWA	Gl(75) + Cpx(25)	0.90	0.62	−12
APR16-C1Ac	1250	1295	45	6	NWA	Gl(83) + Cpx(15) + Ol(2)	2.03	0.83	−20
APR16-C1Ad	1250	1295	45	9	NWA	Gl(90) + Cpx(10)	1.95	0.65	−19
Subseries C1B									
APR16-C1Ba	1200	1295	95	0.25	NWA	Gl(50) + Cpx(41) + Ol(6) + Plg(3)	2.21	0.11	−30
APR16-C1Bb	1200	1295	95	3	NWA	Gl(54) + Cpx(33) + Ol(6) + Plg(7)	2.92	0.38	−40
APR16-C1Bc	1200	1295	95	6	NWA	Gl(57) + Cpx(45) + Plg(2) + Ox(5)	2.72	0.64	−7
APR16-C1Bd	1200	1295	95	9	NWA	Gl(45) + Cpx(37) + Ol(3) + Plg (12) + Ox(3)	2.02	0.84	−4
Series 2									
Subseries C2A									
APR16-C2Aa	1220	1270	50	0.25	2	Gl(91) + Cpx(4) + Ol(1) + Ox(4)	1.92	0.02	−25
APR16-C2Ab	1220	1270	50	3	1.9	Gl(68) + Cpx(23) + Ol(4) + Plg(1) + Ox*	1.56	0.66	−17
APR16-C2Ac	1220	1270	50	6	2.1	Gl(65) + Cpx(27) + Ol(5) + Plg(3)	2.47	0.93	−25
APR16-C2Ad	1220	1270	50	9	1.9	Gl(80) + Cpx(17) + Ol(3) + Ox*	1.30	0.25	−26
Subseries C2B									
APR16-C2Ba	1170	1270	100	0.25	2	Gl(65) + Cpx(29) + Ol(1) + Plg(5)	1.61	3.56	−19
APR16-C2Bb	1170	1270	100	3	2	Gl(63) + Cpx(30) + Ol(6) + Plg(1)	1.39	0.77	−27
APR16-C2Bc	1170	1270	100	6	2	Gl(58) + Cpx(33) + Ol(5) + Plg(1)	3.77	0.73	−27
APR16-C2Bd	1170	1270	100	9	1.8	Gl(57) + Cpx(34) + Ol(2) + Plg(3) + Ox(4)	2.02	0.56	−4
Series 3									
Subseries C3A									
APR16-C3Aa$^{\diamond}$	1080	1218	138	0.25	4	Gl† + Amph + Cpx + Plg + Ox*			
APR16-C3Ab$^{\diamond}$	1080	1218	138	3	4	Gl† + Amph + Cpx + Plg + Ox*			
APR16-C3Ac	1080	1224	144	6	3.8	Gl(60) + Cpx(37) + Ol(3)	6.5	0.62	−10
APR16-C3Ad	1080	1233	153	9	3.3	Gl(55) + Amph(24) + Cpx(20) + Ox(1)	10.2	0.41	−1
Subseries C3B									
APR16-C3Ba$^{\diamond}$	1030	1224	194	0.25	3.8	Gl† + Amph + Cpx + Plg + Ox			
APR16-C3Bb$^{\diamond}$	1030	1225	195	3	3.7	Gl† + Amph + Cpx + Plg + Ox			
APR16-C3Bc$^{\diamond}$	1030	1232	202	6	3.4	Gl† + Amph + Cpx + Opx + Ox			
APR16-C3Bd	1030	1216	186	9	4.2	Gl(40) + Amph(35) + Cpx(24) + Ox(1)	8.3	0.18	−1

Notes: *NWR* natural water rock; *Gl* glass; *Cpx* clinopyroxene; *Ol* olivine; *Plg* plagioclase; *Amph* amphibole; *Ox* oxide. TCpx$_L$ is the equilibrium clinopyroxene liquidus temperature (°C) determined on the basis of phase relations experimental data from Perinelli et al. (2019) and on the calculations by using MELTS software (Ghiorso and Sack 1995; Asimow and Ghiorso 1998). ΔT_{eff} is the difference between the clinopyroxene liquidus temperature and the nominal temperature of the runs. H_2O_i % of water added to the charge. H_2O_f as determined by the *by-difference* calculation method (respect to the total of EMP analyses). Σr^2 values from mass balance calculation. [§] Percent of relative Fe loss from starting material based on difference between the starting material and calculated bulk composition of experiment obtained from mass balance calculations. [†] Phases too small for analysis; *crystals present in trace; [◊] in these runs it was no possible to do mass balance calculation

material, NWA) and at temperatures of 1200 °C (subseries APR16-C1A) and 1250 °C (subseries APR16-C1B). Experiments of *Series 2* (i.e. APR16-C2) were run at hydrous conditions (2 wt.% H_2O added to the starting material), and at temperatures of 1170 °C (subseries APR16-C2A) and 1220 °C (subseries APR16-C2B). Experiments of *Series 3* (i.e. APR16-C3) were run at hydrous conditions (4 wt.% H_2O added to the starting material), and at temperatures of 1080 °C (subseries

APR16-C3A) and 1030 °C (subseries APR16-C3B). Initial water contents and experimental temperatures were chosen on the basis of the melt inclusion studies (Moretti et al. 2013) and phase data were taken from high-pressure anhydrous/hydrous experiments on Procida alkaline basalt magmas as reported in Perinelli et al. (2019).

Finally, because undercooling ($\Delta T = T_{liquidus} - T_{experiment}$) is one of the critical parameters that influences the kinetics of

magma crystallization, we determined the effective undercooling (ΔT_{eff}) for each sample. This is defined as the difference between the equilibrium clinopyroxene liquidus temperature ($TCpx_L$) and the experimental temperature (Hammer and Rutherford 2002). The $TCpx_L$ values used to calculate ΔT_{eff} for each experiment were taken from Procida K-basalt experimental data (Perinelli et al. 2019) and from calculations using MELTS software (Ghiorso and Sack 1995; Asimow and Ghiorso 1998). Resulting $TCpx_L$ and ΔT_{eff} are listed in Table 2.

Analytical techniques

The recovered samples were mounted in epoxy resin, ground flat and polished. Textural aspects of the recovered samples were analysed by Scanning Electron Microscopy (SEM) using a FEI Quanta-400 equipped for microanalysis with an EDAX Genesis system at the Earth Sciences Department (Sapienza University, Rome, Italy). A minimum of eight backscattered electron (BSE) images were acquired for each experimental sample in order to accurately measure the nucleation of clinopyroxene and other crystallized mineral phases (e.g. Clarke et al. 2007; Couch 2003; Hammer et al. 2000). Phase compositions were analysed at the CNR-Istituto di Geologia Ambientale e Geoingegneria (Rome), with a Cameca SX50 electron microprobe equipped with five wavelength disper-sive spectrometers (WDS). Quantitative compositional analy-ses were performed using 15 kV accelerating voltage and 15 nA beam current. As standards we employed metals for Mn and Cr, jadeite for Na, wollastonite for Si and Ca, ortho-clase for K, corundum for Al, magnetite for Fe, rutile for Ti and periclase for Mg. Counting times were 20 s for elements and 10 s for backgrounds. Light elements were counted first to prevent loss by volatilization. The PAP correction method (Pouchou and Pichoir 1991) was used. Minerals were analysed using a beam diameter of 1 μm while for glasses a defocused electron beam of 10 to 15 μm was used. From chemical analyses, the water contents of experimental glasses were estimated according to the by-difference method (Devine et al. 1995). We are aware that this method may result in significant errors in the estimates of H_2O contents in the melts, particularly for H_2O-poor glasses (uncertainty of ~ 0.5 wt.% for $H_2O_{melt} \leq 1$ wt.%; Devine et al. 1995). However, the obtained H_2O values are close to those deter-mined by micro-Raman spectroscopy measurements on resid-ual melts of equilibrium experiments performed on the same composition, at the same P, T and initial hydrous conditions (see Perinelli et al. 2019, for details). Therefore, the H_2O cal-culated using the by-difference method, with EPM analyses, can be considered to be reliable estimates of water contents of experimental melts.

Finally, phase proportions were calculated using bulk and experimental phase compositions and the least squares

regression routine implemented in EXCEL®. Image analysis conducted with ImageJ software was used to estimate the fraction of total solids in each experiment. Estimates of crystal fraction obtained by the latter approach did not produce good results for all samples due to the difficulty in clearly distinguishing the minor phases from glass by applying the thresholding process to backscattered images. However, due to the strong dominance of clinopyroxene in almost all exper-iments, it is reasonable to assume that the clinopyroxene crys-tal fraction (Cpx-ϕ) is representative of the crystallinity of each experiment. Figure S1 in Online Resource 1 displays the comparison of Cpx-ϕ values obtained by the two methods.

Growth rate calculation

In the SEM images, crystal dimensions were measured using the *measure tool* in the ImageJ® software. The maximum growth rate (G_L) values were calculated using a common method reported in literature (Burkhard 2002; Hammer and Rutherford 2002; Couch et al. 2003; Baker 2008; Iezzi et al. 2011):

$$G_L = \frac{(L \cdot W)^{0.5}}{t*2} \tag{1}$$

where L and W are the mean length and width, respectively, of the ten largest crystals for each BSE image (Fig. 1) and t is the duration of the experiments (s). As also shown in the literature, the main growth event often occurs at the beginning of the experiment, since diffusion- or interface-controlled growth nor-mally display lower incremental growth rates as the system approaches equilibrium (e.g. Arzilli et al. 2015; Couch et al. 2003; Orlando et al. 2008). Consequently, long-lasting experi-ments could show an apparent decrease in G_L as time increases.
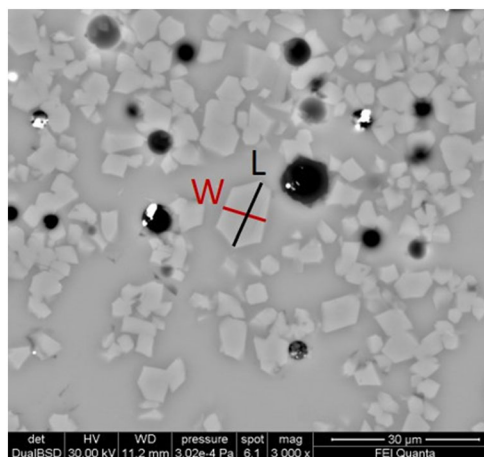

Fig. 1 Backscattered SEM image of a typical experimental result. L and W are the dimensions (i.e. length and width, respectively) that were measured to calculate the growth rate

Crystal size distribution analysis

For textural analyses, we used ImageJ® software (Abramoff et al. 2004; Schneider et al. 2012) on BSE images from which binary images of each mineral were constructed following the procedure described by Philpotts and Ague (2009). Manual reconstruction of edges of overlapping crystals was necessary before conversion into binary images. Subsequently, the data were transferred to the CSDcorrections® software (v. 1.62018; Higgins 2000, 2002) to perform the 2D to 3D conversion and the calculation of CSD plots for each mineral type. Following Higgins (1994), a clinopyroxene aspect ratio of 1:2:2 and a roundness factor of 0.1 were used, and crystals were assumed to have a uniform shape. Indeed, most of the clinopyroxene crystals have an aspect ratio (A, long/short dimension) ranging from one to four with equant habit, while only few crystals have higher aspect ratios ($A \sim 8$) with elongate habits, as shown in Fig. 2 and Fig. S2 in Online Resource 1. The APR16-C1A runs reported in Fig. 2 suggest that crystals tend to start anisotropic (e.g. APR16-C1Aa, APR16-C1Ab) and then become more equant with time (e.g. APR16-C1Ad); this is visible in all the runs (Fig. S2 in Online Resource 1).

The CSD theory (Randolph and Larson 1971; Cashman and Marsh 1988; Marsh 1988) assumes that a steady crystal population grows with a growth rate G (cm·s^{-1}) producing a number of crystals $n(L)$ with length L per unit volume. The total number of crystals is:

$$N(L) = \int_0^L n(L)dL \qquad (2)$$

With a characteristic crystal residence time S, the growth rate is:

$$G = L/S \qquad (3)$$

and the steady variation of population per size interval dL is:

$$dn(L)/dL = -n/G \qquad (4)$$

where n is the number density of crystals.

The integration of Eq. (4) provides:

$$n = n_0\, exp(-L/GS) \qquad (5)$$

that taking the natural logarithm, the relation is:
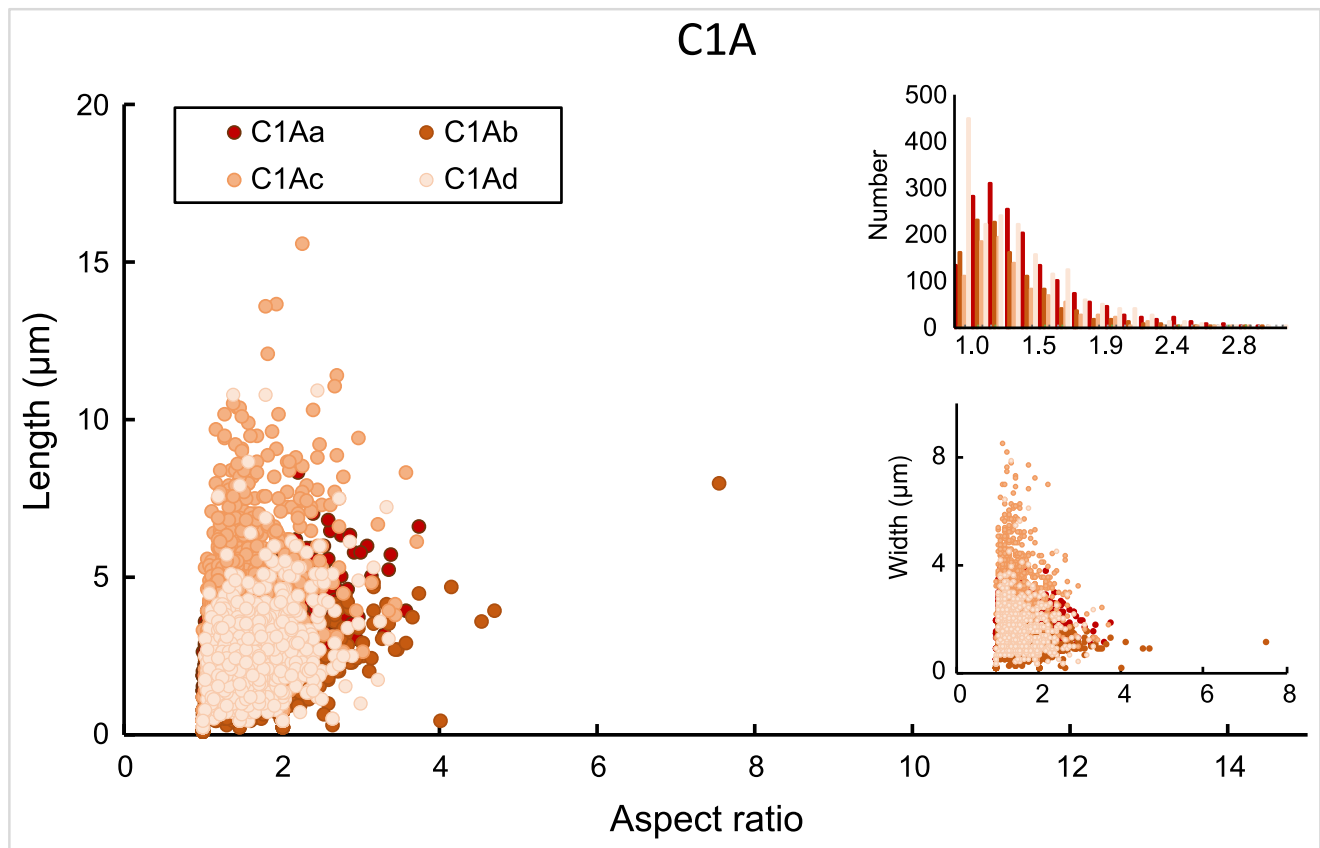
$$\ln(n) = \ln(n_0) - -L/GS \qquad (6)$$

Fig. 2 Length vs. aspect ratio for APR16-C1A runs. We also give the width vs aspect ratio plot (lower inset) and aspect ratio histogram (upper inset)

where n_0 is the number of nuclei at the time of consideration, which is represented here by the time at isothermal conditions. On a plot $ln(n)$ versus L the continuous crystallization ideally provides a linear relation with a slope of $-1/GS$, from which G may be evaluated if S is known, or vice versa. In the same plot, the intercept provides the nucleation density, $ln(n_0)$. The nucleation rate J can now be derived from:

$$J = n_0 G \qquad (7)$$

When the natural logarithm of the population density of crystals varies linearly with the crystal length, CSDs can provide insight into time scales of magmatic processes (e.g. Mangan 1990; Piochi et al. 2005b; Brugger and Hammer 2010a).

Experimental results

BSE images allowed us to identify differences in texture, crystal dimensions and phase abundances as well as to calculate the growth rates of the crystallized phases in each of the experimental *Series* and determine the Crystal Size Distribution (CSD) formed during the experiments.

Phase relations and crystallinity

The experimental products consist of glass and microlites of clinopyroxene (Cpx) ± olivine (Ol) ± plagioclase (Plg) ± oxide

(Ox) ± amphibole (Amph). Small bubbles dispersed within the residual glasses or grouped along the capsule walls are frequently observed in the experiments at H_2O-undersaturated conditions, that for the Procida K-basalt magmas occur when water content in the melt is < 8 wt.% (Perinelli et al. 2019). These bubbles were probably trapped within the glassy powder during the experimental charge preparation, and served as nucleation sites, as testified by the crystal clusters around them.

Phase relations obtained from the three experimental *Series* are shown in the diagram T vs water content in the residual glasses (H_2O_f; Fig. 3). The mineral assemblage as well as the phase abundances obtained in the long experiments (6 and 9 h) generally matches those obtained from equilibrium experiments reported by Perinelli et al. (2019; see Table S1 in Online Resource 2).

For our study, mass balance calculations indicate variable crystallization degrees within each subseries of experiments showing, as a general rule, crystallinity increasing with time (Table 2). Exceptions are the APR16-C1A (NWA, 1250 °C runs) and APR16-C2A (H_2O_i = 2 wt.%, 1220 °C runs) subseries, in which the initial increase of crystal fraction is followed by a significant decline in mineral abundance (i.e. runs at 9 h of dwell time; Table 2). In contrast, crystallization data determined from backscattered image analyses indicate higher degrees of crystallization than those determined by mass balance calculations and a similar crystallinity between runs of 3, 6

Fig. 3 Phase relation data from this experimental study plotted in the diagram of temperature vs. water content in the melt phase (H_2O_f). The diagram reports experimental saturation curves (dashed when estimated), phase assemblages and stability fields at 0.8 GPa, for K-basaltic scoria clasts of the Solchiaro deposit and APR16GL (modified after Perinelli et al. 2019). Black stars are the experiments in which the crystallized mineral assemblage matches that obtained in the equilibrium experiments of Perinelli et al. (2019). Phase abbreviations are Liq: liquid; Cpx: clinopyroxene; Ol: olivine; Ox: oxide; Plg: plagioclase; Opx: orthopyroxene and Amph: amphibole
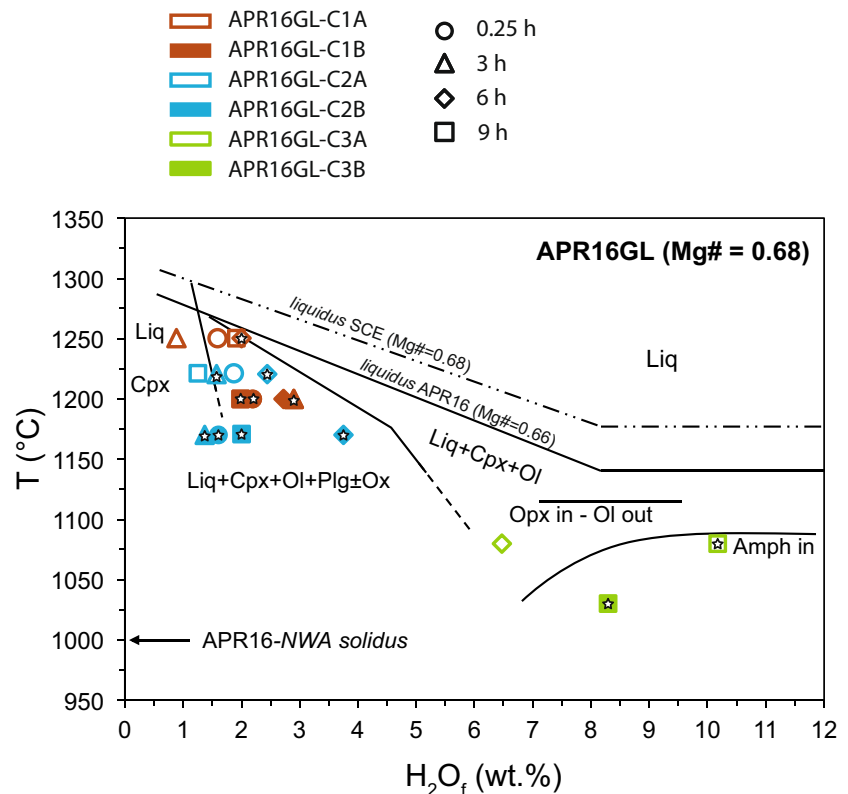
and 9 h for both the APR16-C1A and APR16-C2A subseries (Fig. S1 in Online Resource 1). Image analysis also shows a good correspondence between the mass balance versus image analyses for Cpx-φ values of the APR16-C1B (NWA, 1200 °C runs) and APR16-C2B (H2Oi = 2 wt.%, 1170 °C runs) subseries (Fig. S1 in Online Resource 1). This is probably related to the high undercooling ($\Delta T_{eff} \sim 100$ °C) for both the APR16-C1B and APR16-C2B experimental subseries, which drives the melt towards a crystallization degree approaching that of equilibrium conditions (Lesher et al. 1999; Conte et al. 2006; Hammer 2008). Concerning the APR16-C1A and APR16-C2A subseries experiments, several lines of evidence suggest that heterogeneous nucleation is the general rule in all experiments (i.e. preferential nucleation of clinopyroxenes along the capsule surfaces or around small bubbles, Fig. S3 in Online Resource 1). In heterogeneous nucleation, the nuclei growing on pre-existing surfaces in the liquid require less energy to reach the critical size than that required for homogeneous nucleation (Cashman 1993), where the appearance of new crystals is promoted. Thus, for the APR16-C1A and APR16-C2A experimental subseries, the variation in crystallization degree and phase relations can be explained by heterogeneous nucleation that promoted crystallization of a specific mineral phase at the expense of the others, or influenced the crystal-melt distribution along the wall of sample holder producing chemical inhomogeneities of residual glass that were not completely equilibrated.

Textural features of the experimental runs

Experimental textures of the three *Series* show limited variations mainly linked to the increase of crystal abundance in the charge. In general, relatively large pools of residual glass ($\geq$ 50×50 μm in size; Fig. S3-S4 in Online Resource 1) are
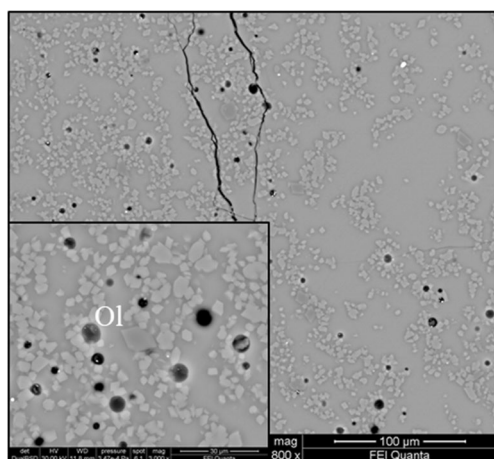

Fig. 4 Backscattered SEM image of an olivine crystal showing a euhedral habit with well-faceted faces from run APR16-C1Ac of *Series 1*

confined to the boundary of sample holder and crystal aggregation is observed (Fig. S4-S5 in Online Resource 1).

Series 1 In the runs of the subseries APR16-C1A (1250 °C, NWA; Fig. S3a in Online Resource 1), the dominant phase is Cpx while olivine (Ol) crystallizes only in the APR16-C1Ac run at 6 h (Table 2). The habit and sizes of Cpx vary with time: subhedral grains with sizes of 5 μm occur in the shortest run (APR16-C1Aa; 0.25 h), while those that are euhedral in shape and up to 15 μm in size appear in the run with longest duration (APR16-C1Ad; 9 h). Olivine is euhedral with well-faceted faces and sizes of ~ 10 μm (Fig. 4).

The runs of the subseries APR16-C1B (1200 °C, NWA; Fig. S3b in Online Resource 1) show a higher degree of crystallization than those of the APR16-C1A subseries and the mineral assemblage consists of Cpx + Ol + Plg + Ox. In the run with shortest duration (APR16-C1Ba; 0.25 h), Cpx is present as subhedral crystals, sometimes forming aggregates. With increasing duration, Cpx develops euhedral habits with sizes up to 20 μm. Similarly, Plg forms large tabular crystals (up to ~ 100 μm in length and ~ 30 μm in width) in the run with longest duration (APR16-C1Bd; 9 h). Olivine and Ox (present only in the runs at 6 and 9 h) have euhedral habits with sizes of ~ 25 and 15 μm, respectively. Some Ox crystals are characterized by a Cr-rich core.

Series 2 The mineral phases crystallized in subseries APR16-C2A (1220 °C, 2 wt.% H2Oi; Fig. S4a in Online Resource 1) are the same as those that crystallized in subseries APR16-C1B. Clinopyroxene and Ol are ubiquitous in these runs, whereas Plg is present only in the runs at 3 and 6 h and Ox is absent in the run at 6 h. Clinopyroxene shows a subhedral habit in the run with shortest duration and is euhedral in the other runs, with sizes between ~ 10 and 20 μm. Olivine crystals are well-faceted with sizes of ~ 15 μm; occasionally they contain embayments. Plg is euhedral with sizes up to ~ 40 μm.

The runs of the subseries APR16-C2B (1170 °C, 2 wt.% H2Oi) show a higher degree of crystallization (Fig. S4b in Online Resource 1) and the mineral assemblage is Cpx + Ol + Plg ± Ox (Table 2). Clinopyroxene, Ol and Plg crystallize in all the runs, while Ox occurs only in the longest run (APR16-C2Bd; 9 h). Textural features are very similar to subseries APR16-C1B.

Series 3 In the runs of subseries APR16-C3A (1080 °C, 4 wt.% H2Oi; Fig. S5a in Online Resource 1) and APR16-C3B (1030 °C, 4 wt.% H2Oi; Fig. S5b in Online Resource 1), the main phase is Amph, which is ubiquitous. The runs with the shortest durations (APR16-C3Aa, APR16-C3Ba and APR16-C3Ab, APR16-C3Bb; 0.25 and 3 h, respectively) are characterized by an extensive distribution of tiny crystals, most of them smaller than 10 μm in size, frequently occurring in crystalline aggregates (Fig. S5 in Online Resource 1). Small
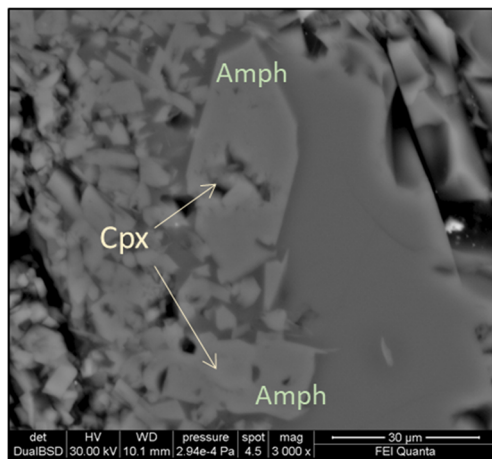
Fig. 5 Backscattered SEM images of Cpx crystals constituting the core of Amph from run APR16-C3Ad of *Series 3*

plugs of glass occasionally occur at the edge of these aggregates, but they are too small to be accurately analysed. The runs with the longest duration (APR16-C3Ad and APR16-C3Bd, 9 h) are characterized by the crystallization of Amph, Cpx and Ox. Clinopyroxene crystals are euhedral, up to ~
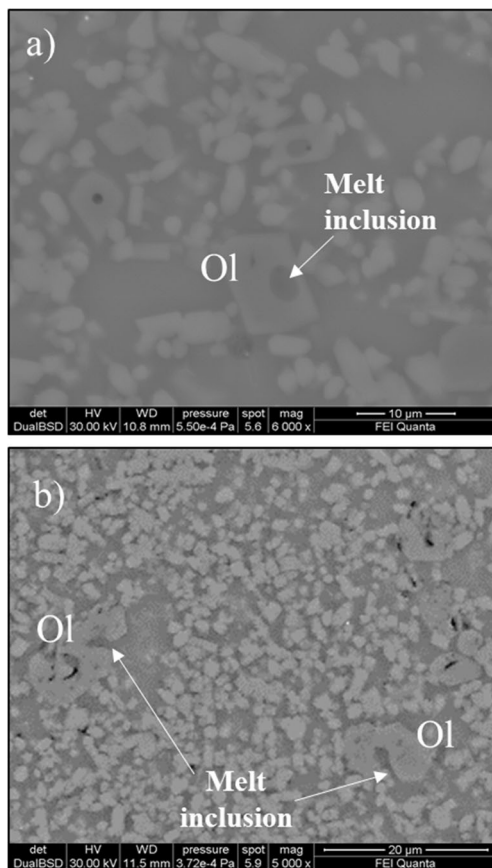

Fig. 6 Backscattered SEM images of polyhedral Ol crystals containing embayments formed in run APR16-C2Bc of *Series 2*. **a** Closed melt inclusion isolated inside their host crystals. **b** Open melt inclusions extending to the crystal rim through a narrow or wide neck

5 μm in size, and sometimes constitute the core of Amph crystals (Fig. 5). Amphibole and Ox show euhedral habits with sizes up to ~ 60 and 40 μm, respectively.

An interesting feature concerns Ol crystals, which has a morphology that can be described as polyhedral, according to the classification of Faure et al. (2003). Polyhedral Ol crystals contain embayments or cavities, formed during multiple growth steps (Faure and Schiano 2005); these polyhedral habits were found in several experimental runs (e.g. APR16-C2Bb, APR16-C2Bc, APR16-C2Bd). In particular, it was possible to recognize (i) melt inclusions isolated inside their host crystals, with sizes between 1 and 3 μm, and shapes that can be spherical, sub-spherical or ovoid, up to irregular but still curvilinear (Fig. 6a); and (ii) open melt inclusions (embayments) extending to the crystal rim through a narrow or wide neck (Fig. 6b). This type of texture is sometimes interpreted as resulting from processes unrelated to the growth of the host crystal (e.g. chemical resorption due to crystal-melt disequilibria or thermal erosion at the crystal-liquid interface associated with transport in the magma conduit; Helz and Wright 1992; Thornber 2001; Pan and Batiza 2002). However, in our experiments, as found by Faure and Schiano (2005), this embayed texture was formed during olivine crystal growth under near-equilibrium conditions.

Clinopyroxene composition and approach to equilibrium

Chemical compositions of clinopyroxene and glass are given in Table S2 in Online Resource 2. Clinopyroxene crystals are augitic (Wo_{42}-En_{41}-Fs_{18}) and diopsidic (Wo_{47}-En_{43}-Fs_{10}) in composition according to the classification scheme of

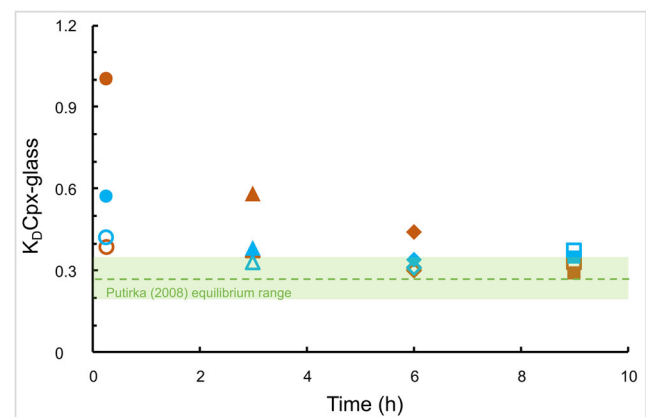**Fig. 7** Relation between K_D(Fe-Mg)$^{Cpx-liq}$ and time. The duration of each run is indicated with different symbols: circles for 0.25 h runs, triangles for 3 h runs, diamonds for 6 h runs and squares for 9 h runs. *Series* are indicated with different colours: red for APR16-C1, light blue for APR16-C2. Within each series, subseries are indicated with full (runs at lower temperature) and empty (runs at higher temperature) symbols. The green field represents the equilibrium range according to Putirka (2008), while the dotted line represents the average K_D value for Cpx (0.28 ± 0.08; Putirka (2008))

Morimoto et al. ([1998](#)). Overall, the Mg# of Cpx (calculated as the molar MgO/(MgO + FeO$_{tot}$) ratio) varies between 0.76 and 0.88, while the Mg# of glass lies between 0.52 and 0.77. The Fe–Mg distribution coefficients between clinopyroxene and melt $(K_D(Fe\text{-}Mg)^{Cpx\text{-}liq} = Fe_{Cpx} \times Mg_{liq}/Mg_{Cpx} \times Fe_{liq}$, calculated assuming all Fe as Fe^{2+} in both phases) varies between 0.39 ± 0.05 and 0.30 ± 0.05 for APR16-C1A runs, 1.00 ± 0.10 and 0.29 ± 0.01 for APR16-C1B runs, 0.43 ± 0.06 and 0.31 ± 0.06 for APR16-C2A runs, and 0.57 ± 0.06 and 0.34 ± 0.04 for APR16-C2B runs. As shown in Fig. 7, all the shortest experiments, and in particular those of the subseries APR16-C1B and APR16-C2B, show significant deviation from the equilibrium range $(K_D(Fe\text{-}Mg)^{Cpx\text{-}liq} = 0.28 \pm 0.08$ according to Putirka ([2008](#))), while runs of 3 h or more increasingly reach equilibrium conditions.

Crystal growth rates

Maximum growth rates determined for clinopyroxene are reported in Table 3, and Fig. 8 shows the relationships between (a) crystal size (L) and experimental duration, and (b) crystal growth rate (G$_L$) and experiment duration. In *Series 1*, we observed an increase in crystal size with increasing experiment duration. Moreover, Cpx in APR16-C1A runs at 1250 °C are smaller than in APR16-C1B runs at 1200 °C. As regards crystal growth rates, the obtained values decrease by about an order of magnitude with increasing duration of the experiments, decreasing from 10^{-7} to 10^{-8} cm·s^{-1} as duration increases from 0.25 to 9 h. Within each series, G$_L$ calculated from experiments at higher temperatures are slightly lower than those obtained from experiments at lower temperatures (Fig. 8b). *G*rowth rates calculated

Table 3 Calculated growth rate values for clinopyroxene

Run #	T (°C)	Time (s)	H$_2$O$_f$ (wt.%)	L (cm)	St. dev. (cm)	W (cm)	St. dev. (cm)	G$_L$ (cm·s^{-1})	St. dev. (cm·s^{-1})
Series 1									
Subseries C1A									
APR16-C1Aa	1250	900	1.61	$6.48 \cdot 10^{-04}$	$4.4 \cdot 10^{-05}$	$3.13 \cdot 10^{-04}$	$6.8 \cdot 10^{-05}$	$2.50 \cdot 10^{-07}$	$2.9 \cdot 10^{-08}$
APR16-C1Ab	1250	10,800	2.33	$1.17 \cdot 10^{-03}$	$2.1 \cdot 10^{-04}$	$5.30 \cdot 10^{-04}$	$9.8 \cdot 10^{-05}$	$3.64 \cdot 10^{-08}$	$6.8 \cdot 10^{-09}$
APR16-C1Ac	1250	21,600	2.03	$1.35 \cdot 10^{-03}$	$1.5 \cdot 10^{-04}$	$5.86 \cdot 10^{-04}$	$1.5 \cdot 10^{-04}$	$2.06 \cdot 10^{-08}$	$2.8 \cdot 10^{-09}$
APR16-C1Ad	1250	32,400	1.95	$1.43 \cdot 10^{-03}$	$2.1 \cdot 10^{-04}$	$8.78 \cdot 10^{-04}$	$1.2 \cdot 10^{-04}$	$1.73 \cdot 10^{-08}$	$2.0 \cdot 10^{-09}$
Subseries C1B									
APR16-C1Ba	1200	900	2.21	$1.05 \cdot 10^{-03}$	$1.4 \cdot 10^{-04}$	$4.86 \cdot 10^{-04}$	$1.6 \cdot 10^{-04}$	$3.96 \cdot 10^{-07}$	$7.0 \cdot 10^{-08}$
APR16-C1Bb	1200	10,800	2.92	$1.52 \cdot 10^{-03}$	$2.5 \cdot 10^{-04}$	$9.85 \cdot 10^{-04}$	$2.5 \cdot 10^{-04}$	$5.67 \cdot 10^{-08}$	$1.1 \cdot 10^{-08}$
APR16-C1Bc	1200	21,600	2.72	$1.85 \cdot 10^{-03}$	$1.6 \cdot 10^{-04}$	$1.50 \cdot 10^{-03}$	$4.4 \cdot 10^{-04}$	$3.86 \cdot 10^{-08}$	$6.8 \cdot 10^{-09}$
APR16-C1Bd	1200	32,400	2.02	$1.93 \cdot 10^{-03}$	$2.3 \cdot 10^{-04}$	$1.32 \cdot 10^{-03}$	$3.9 \cdot 10^{-04}$	$2.46 \cdot 10^{-08}$	$5.2 \cdot 10^{-09}$
Series 2									
Subseries C2A									
APR16-C2Aa	1220	900	1.92	$8.40 \cdot 10^{-04}$	$1.1 \cdot 10^{-04}$	$4.05 \cdot 10^{-04}$	$9.2 \cdot 10^{-05}$	$3.24 \cdot 10^{-07}$	$5.2 \cdot 10^{-08}$
APR16-C2Ab	1220	10,800	1.56	$1.07 \cdot 10^{-03}$	$2.3 \cdot 10^{-04}$	$4.04 \cdot 10^{-04}$	$6.5 \cdot 10^{-05}$	$3.04 \cdot 10^{-08}$	$3.9 \cdot 10^{-09}$
APR16-C2Ac	1220	21,600	2.47	$1.68 \cdot 10^{-03}$	$1.3 \cdot 10^{-04}$	$7.93 \cdot 10^{-04}$	$3.0 \cdot 10^{-04}$	$2.67 \cdot 10^{-08}$	$5.1 \cdot 10^{-09}$
APR16-C2Ad	1220	32,400	1.30	$1.70 \cdot 10^{-03}$	$1.6 \cdot 10^{-04}$	$9.22 \cdot 10^{-04}$	$2.0 \cdot 10^{-04}$	$1.93 \cdot 10^{-08}$	$2.2 \cdot 10^{-09}$
Subseries C2B									
APR16-C2Ba	1170	900	1.61	$9.98 \cdot 10^{-04}$	$2.1 \cdot 10^{-04}$	$4.20 \cdot 10^{-04}$	$9.8 \cdot 10^{-05}$	$3.60 \cdot 10^{-07}$	$4.6 \cdot 10^{-08}$
APR16-C2Bb	1170	10,800	1.39	$1.57 \cdot 10^{-03}$	$1.0 \cdot 10^{-04}$	$6.06 \cdot 10^{-04}$	$3.6 \cdot 10^{-04}$	$4.52 \cdot 10^{-08}$	$1.2 \cdot 10^{-08}$
APR16-C2Bc	1170	21,600	3.77	$1.80 \cdot 10^{-03}$	$1.0 \cdot 10^{-04}$	$7.94 \cdot 10^{-04}$	$3.5 \cdot 10^{-04}$	$2.77 \cdot 10^{-08}$	$5.8 \cdot 10^{-09}$
APR16-C2Bd	1170	32,400	2.02	$1.97 \cdot 10^{-03}$	$1.8 \cdot 10^{-04}$	$1.17 \cdot 10^{-03}$	$6.1 \cdot 10^{-04}$	$2.34 \cdot 10^{-08}$	$7.0 \cdot 10^{-09}$
Series 3									
Subseries C3A									
APR16-C3Ab	1080	10,800		$5.38 \cdot 10^{-04}$	$5.0 \cdot 10^{-05}$	$3.50 \cdot 10^{-04}$	$5.2 \cdot 10^{-05}$	$2.01 \cdot 10^{-08}$	$7.0 \cdot 10^{-10}$
APR16-C3Ac	1080	21,600	6.5	$7.45 \cdot 10^{-04}$	$1.8 \cdot 10^{-04}$	$4.28 \cdot 10^{-04}$	$5.7 \cdot 10^{-05}$	$1.31 \cdot 10^{-08}$	$2.5 \cdot 10^{-09}$
APR16-C3Ad	1080	32,400	10.2	$5.44 \cdot 10^{-04}$	$7.7 \cdot 10^{-05}$	$4.26 \cdot 10^{-04}$	$4.8 \cdot 10^{-05}$	$7.43 \cdot 10^{-09}$	$8.4 \cdot 10^{-10}$
Subseries C3B									
APR16-C3Bc	1030	21,600		$6.43 \cdot 10^{-04}$	$7.8 \cdot 10^{-05}$	$5.55 \cdot 10^{-04}$	$6.0 \cdot 10^{-05}$	$1.38 \cdot 10^{-08}$	$1.3 \cdot 10^{-09}$
APR16-C3Bd	1030	32,400	8.3	$5.70 \cdot 10^{-04}$	$6.6 \cdot 10^{-05}$	$5.00 \cdot 10^{-04}$	$3.4 \cdot 10^{-05}$	$8.24 \cdot 10^{-09}$	$5.3 \cdot 10^{-10}$

Notes: *NWA* natural water rock; H$_2$O$_f$ as determined by the *by-difference* calculation method (respect to the total of EMP analyses). *L* and *W* are the length and the width of the crystals. *G*$_L$ is the calculated growth rate. *St. dev.* standard deviation

Fig. 8 Relation between **a** Cpx size (*L*) and experimental duration, and **b** Cpx growth rate (*G*$_L$) and experimental duration (*t*). The duration of the runs is indicated with different symbols: circle for 0.25 h runs, triangle for 3 h runs, diamond for 6 h runs and square for 9 h runs. *Series* are indicated with different colours: red for APR16-C1, light blue for APR16-C2 and green for APR16-C3. Within each series, each sub-series is indicated with full (runs at lower temperature) and empty (runs at higher temperature) symbols. In Fig. 8b, the error bars are not shown since they are inside the symbols
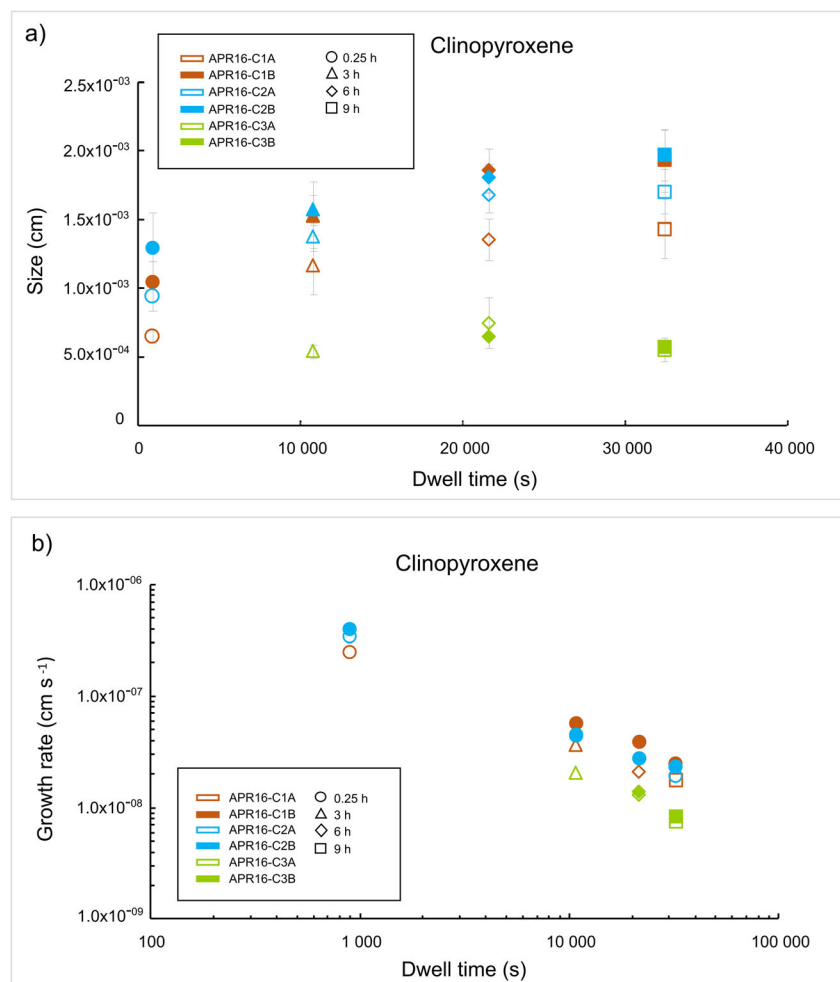
for other phases are in Table 4. As seen for clinopyroxene, the calculated growth rates of all other phases decrease with increasing time. For both Ol (Fig. 9a) and Plg (Fig. 9b), G_L decreases from about 10^{-6} to 10^{-8} cm·s^{-1} (Table 4) as time increases from 0.25 to 9 h. For Amph and Ox, we were able to calculate the growth rates only for the runs with duration ≥ 3 h, and these had values of ∼ 10^{-8} cm·s^{-1} (Table 4).

Crystal size distribution analysis

The CSDs calculated for the APR16GL runs of *Series 1* and *2* are shown in Fig. 10a–d. For the runs of *Series 3*, it was not possible to perform CSD analysis due to the small size of the Cpx (which was below the detection limit). CSD theory predicts that steady-state conditions of continuous nucleation and growth will produce a linear CSD plot with a negative slope, while deviations from linearity suggest the involvement of other processes (Cashman and Marsh 1988; Marsh 1988, 1998; Lentz and Mcsween 2000). For instance, a turnover at the smallest grain sizes may be due to (i) a complete cessation of nucleation with continued growth that favours the growth of the smallest grains in the next largest bin sizes, but with no

replacements produced by nucleation (Lentz and Mcsween 2000); (ii) annealing that causes absorption of small grains with balancing growth of larger ones (Lentz and Mcsween 2000); and/or (iii) a limitation to the imaging technique (Marsh 1988). Another possible deviation from linearity is an increase of the largest grain sizes that implies an excess of large grains compared with smaller sizes; this may be due to accumulation or addition of large phenocrysts (Marsh 1988). All runs suitable for CSD analysis show similar curves. In the longest runs (6–9 h), in particular, CSDs yield two best-fit lines with different slopes: a gentler slope for coarser crystals and a steeper slope for the smallest crystals (< 8 μm in size). Moreover, a reduction in both slope and intercept leads to a counter-clockwise rotation of the CSD with time (Fig. 10a–d), which indicates an absence of new nucleation (Ni et al. 2014). Small crystals may also partly or completely dissolve due to their higher surface energies, which causes their population density to fall below the log-linear CSD curve (Ni et al. 2014). Moreover, by using the growth rates calculated in this work for the APR16 runs, we estimated nucleation rates J ($J = n_0 G_L$) of 10^5 and 10^3 mm^{-3}·s^{-1} in the run with the shortest (0.25 h) and the longest (9 h) durations, respectively (Table S3 in Online Resource 2).

Table 4 Calculated growth rate values for olivine, plagioclase, amphibole and oxide

Run #	T (°C)	Time (s)	H_2O_f (wt%)	Phase	L (cm)	St. dev. (cm)	W (cm)	St. dev. (cm)	G_L (cm·s^{-1})	St. dev. (cm·s^{-1})
Series 1										
Subseries C1A										
APR16-C1Ba	1200	900	2.21	Ol	$2.49 \cdot 10^{-03}$	$3.4 \cdot 10^{-04}$	$1.89 \cdot 10^{-03}$	$5.0 \cdot 10^{-04}$	$1.21 \cdot 10^{-06}$	$2.4 \cdot 10^{-07}$
				Plg	$1.38 \cdot 10^{-03}$	$2.3 \cdot 10^{-04}$	$8.48 \cdot 10^{-04}$	$9.4 \cdot 10^{-05}$	$6.01 \cdot 10^{-07}$	$6.5 \cdot 10^{-08}$
APR16-C1Bb	1200	10,800	2.92	Ol	$2.96 \cdot 10^{-03}$	$1.8 \cdot 10^{-03}$	$1.01 \cdot 10^{-03}$	$5.7 \cdot 10^{-05}$	$8.00 \cdot 10^{-08}$	$2.7 \cdot 10^{-08}$
				Plg	$1.78 \cdot 10^{-03}$	$4.0 \cdot 10^{-05}$	$8.23 \cdot 10^{-04}$	$4.5 \cdot 10^{-05}$	$5.60 \cdot 10^{-08}$	$2.2 \cdot 10^{-09}$
APR16-C1Bc	1200	21,600	2.72	Plg	$1.95 \cdot 10^{-03}$	$3.1 \cdot 10^{-04}$	$9.98 \cdot 10^{-04}$	$8.5 \cdot 10^{-05}$	$3.23 \cdot 10^{-06}$	$3.7 \cdot 10^{-09}$
				Ox	$1.41 \cdot 10^{-03}$	$1.8 \cdot 10^{-04}$	$1.06 \cdot 10^{-03}$	$1.5 \cdot 10^{-04}$	$2.83 \cdot 10^{-08}$	$3.4 \cdot 10^{-09}$
APR16-C1Bd	1200	32,400	2.02	Ol	$2.28 \cdot 10^{-03}$	$5.3 \cdot 10^{-04}$	$1.27 \cdot 10^{-03}$	$3.2 \cdot 10^{-04}$	$2.63 \cdot 10^{-08}$	$5.7 \cdot 10^{-09}$
				Plg	$7.82 \cdot 10^{-03}$	$2.2 \cdot 10^{-03}$	$2.71 \cdot 10^{-03}$	$1.1 \cdot 10^{-03}$	$7.11 \cdot 10^{-08}$	$1.7 \cdot 10^{-08}$
				Ox	$1.87 \cdot 10^{-03}$	$2.4 \cdot 10^{-04}$	$1.54 \cdot 10^{-03}$	$2.2 \cdot 10^{-04}$	$2.62 \cdot 10^{-08}$	$3.5 \cdot 10^{-09}$
Series 2										
Subseries C2A										
APR16-C2Aa	1220	900	1.92	Ol	$4.47 \cdot 10^{-03}$	$5.4 \cdot 10^{-04}$	$2.75 \cdot 10^{-03}$	$4.1 \cdot 10^{-04}$	$1.95 \cdot 10^{-06}$	$2.3 \cdot 10^{-07}$
APR16-C2Ab	1220	10,800	1.56	Ol	$1.48 \cdot 10^{-03}$	$4.5 \cdot 10^{-04}$	$6.89 \cdot 10^{-04}$	$1.7 \cdot 10^{-04}$	$4.67 \cdot 10^{-08}$	$1.2 \cdot 10^{-08}$
				Plg	$4.56 \cdot 10^{-03}$	$7.0 \cdot 10^{-04}$	$2.03 \cdot 10^{-03}$	$3.5 \cdot 10^{-04}$	$1.41 \cdot 10^{-07}$	$2.2 \cdot 10^{-08}$
APR16-C2Ac	1220	21,600	2.47	Ol	$1.49 \cdot 10^{-03}$	$2.0 \cdot 10^{-04}$	$1.18 \cdot 10^{-04}$	$1.1 \cdot 10^{-04}$	$3.07 \cdot 10^{-08}$	$3.0 \cdot 10^{-09}$
				Plg	$5.36 \cdot 10^{-08}$	$1.1 \cdot 10^{-03}$	$1.35 \cdot 10^{-03}$	$1.3 \cdot 10^{-04}$	$5.36 \cdot 10^{-08}$	$9.7 \cdot 10^{-09}$
APR16-C2Ad	1220	32,400	1.30	Ol	$1.55 \cdot 10^{-03}$	$2.5 \cdot 10^{-04}$	$1.34 \cdot 10^{-04}$	$2.0 \cdot 10^{-04}$	$2.22 \cdot 10^{-08}$	$1.6 \cdot 10^{-07}$
Subseries C2B										
APR16-C2Ba	1170	900	1.61	Plg	$2.14 \cdot 10^{-03}$	$4.3 \cdot 10^{-04}$	$9.57 \cdot 10^{-04}$	$1.0 \cdot 10^{-04}$	$7.95 \cdot 10^{-07}$	$1.0 \cdot 10^{-07}$
APR16-C2Bb	1170	10,800	1.39	Ol	$9.78 \cdot 10^{-04}$	$7.6 \cdot 10^{-01}$	$8.44 \cdot 10^{-04}$	$5.7 \cdot 10^{-05}$	$4.21 \cdot 10^{-08}$	$3.0 \cdot 10^{-09}$
APR16-C2Bc	1170	21,600	3.77	Ol	$1.39 \cdot 10^{-03}$	$2.5 \cdot 10^{-04}$	$1.12 \cdot 10^{-03}$	$1.8 \cdot 10^{-04}$	$2.88 \cdot 10^{-08}$	$4.5 \cdot 10^{-09}$
				Plg	$4.10 \cdot 10^{-03}$	$1.6 \cdot 10^{-03}$	$1.90 \cdot 10^{-03}$	$7.1 \cdot 10^{-04}$	$6.46 \cdot 10^{-08}$	$2.4 \cdot 10^{-08}$
APR16-C2Bd	1170	32,400	2.02	Ol	$1.18 \cdot 10^{-03}$	$9.7 \cdot 10^{-05}$	$1.04 \cdot 10^{-03}$	$5.3 \cdot 10^{-05}$	$1.71 \cdot 10^{-08}$	$1.1 \cdot 10^{-09}$
				Plg	$1.55 \cdot 10^{-03}$	$7.1 \cdot 10^{-05}$	$7.50 \cdot 10^{-04}$	$7.1 \cdot 10^{-05}$	$1.66 \cdot 10^{-08}$	$1.2 \cdot 10^{-09}$
Series 3										
Subseries C3A										
APR16-C3Ab	1080	10,800		Amph	$2.59 \cdot 10^{-03}$	$6.8 \cdot 10^{-04}$	$7.50 \cdot 10^{-04}$	$2.1 \cdot 10^{-04}$	$6.45 \cdot 10^{-08}$	$1.4 \cdot 10^{-08}$
APR16-C3Ac	1080	21,600	6.5	Ol	$4.52 \cdot 10^{-03}$	$6.4 \cdot 10^{-04}$	$2.15 \cdot 10^{-03}$	$4.9 \cdot 10^{-04}$	$7.21 \cdot 10^{-08}$	$7.4 \cdot 10^{-09}$
APR16-C3Ad	1080	32,400	10.2	Amph	$3.26 \cdot 10^{-03}$	$1.3 \cdot 10^{-03}$	$1.16 \cdot 10^{-03}$	$4.1 \cdot 10^{-04}$	$2.99 \cdot 10^{-08}$	$1.0 \cdot 10^{-08}$
				Ox	$3.09 \cdot 10^{-03}$	$8.7 \cdot 10^{-04}$	$2.57 \cdot 10^{-03}$	$1.1 \cdot 10^{-03}$	$4.34 \cdot 10^{-08}$	$1.5 \cdot 10^{-08}$
Subseries C3B										
APR16-C3Bc	1030	21,600		Amph	$1.90 \cdot 10^{-03}$	$2.5 \cdot 10^{-04}$	$6.77 \cdot 10^{-04}$	$7.5 \cdot 10^{-05}$	$2.63 \cdot 10^{-08}$	$1.8 \cdot 10^{-09}$
				Ox	$8.68 \cdot 10^{-04}$	$1.0 \cdot 10^{-04}$	$8.00 \cdot 10^{-04}$	$9.6 \cdot 10^{-05}$	$1.93 \cdot 10^{-08}$	$2.3 \cdot 10^{-09}$
APR16-C3Bd	1030	32,400	8.23	Amph	$3.32 \cdot 10^{-03}$	$6.0 \cdot 10^{-04}$	$1.04 \cdot 10^{-03}$	$2.9 \cdot 10^{-04}$	$2.86 \cdot 10^{-08}$	$4.0 \cdot 10^{-09}$
				Ox	$1.53 \cdot 10^{-03}$	$2.7 \cdot 10^{-04}$	$1.42 \cdot 10^{-03}$	$2.6 \cdot 10^{-04}$	$2.28 \cdot 10^{-08}$	$4.0 \cdot 10^{-09}$

Notes: *NWA* natural water rock; *Ol* olivine; *Plg* plagioclase; *Amph* amphibole; *Ox* oxide. H_2O_f as determined by the *by-difference* calculation method (respect to the total of EMP analyses). L and W are the length and the width of the crystals. G_L is the calculated growth rate. *St. dev.* standard deviation

Discussion

Chemical and crystal fraction equilibrium of experimental clinopyroxene

Putirka (1999) and Putirka et al. (2003) have demonstrated that Fe–Mg exchange between clinopyroxene and the melt ($K_D(\text{Fe-Mg})^{Cpx\text{-}liq} = \text{Fe}_{Cpx} \times \text{Mg}_{liq}/\text{Mg}_{Cpx} \times \text{Fe}_{liq}$) can be extremely useful for the assessment of equilibrium conditions. The $K_D(\text{Fe-Mg})^{Cpx\text{-}liq}$ calculated for our experimental runs show that chemical equilibrium was reached at between 3 and 6 h. In order to observe if the crystal fraction equilibrium is achieved in the same amount of time as the chemical equilibrium, we plotted clinopyroxene fraction and against experimental dwell time (Fig. 11). In Fig. 11a, we observed a rapid increase in Cpx-ϕ, and increase that occurs in the

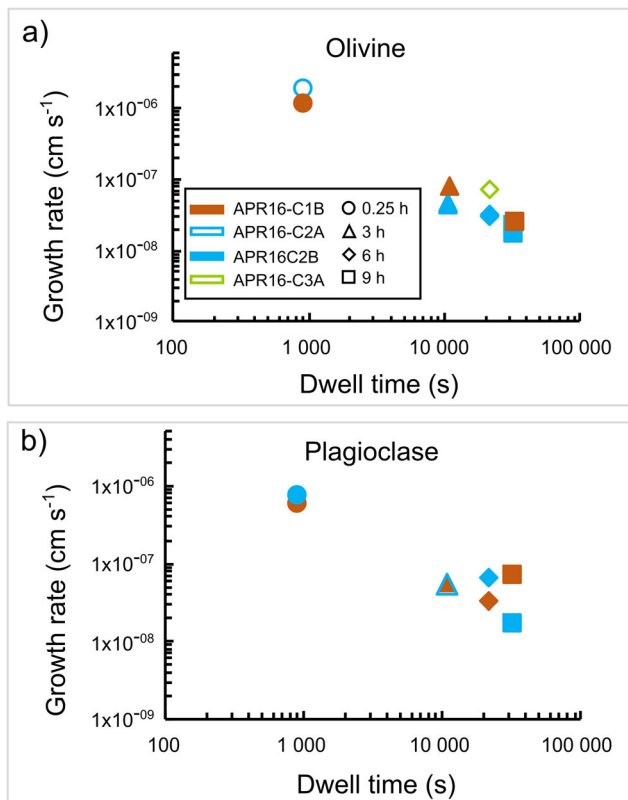**Fig. 9** Relation between the growth rate (G_L) and the experiment duration (t) for olivine (**a**) and plagioclase (**b**). Symbols are as in Fig. 8. Error bars in Fig. 9b are not shown since they are inside the symbols

first 15 min, after which Cpx-ϕ remains approximately constant. In the APR16-C1A and APR16-C2A experiments, however, Cpx-ϕ increases for up to 3 h before approaching a constant value, suggesting an approach to crystal fraction equilibrium conditions (Fig. 11a). This trend is similar to those obtained in previous studies (Melnik and Sparks 2005; Polacci et al. 2018), in which the crystal content initially increases rapidly, and then increases less slowly, but linearly, until it reaches equilibrium. Moreover, evolution towards equilibrium is also testified by the decrease in the crystallization rate with time (Fig. 11b). Thus, our experiments show that for Procida K-basalt magmas, independently of ΔT_{eff} and for $H_2O_i \leq 2$ wt.%, the approach to clinopyroxene equilibrium (both chemical and crystal fraction) occurs after 3 h of dwell time.

Growth rate dependence on time

As observed in previous studies (e.g. Hammer and Rutherford 2002; Couch 2003; Arzilli and Carroll 2013; Arzilli et al. 2015), time plays a key role in the crystallization processes of silicate melts. The effective Cpx growth rate calculated in this work varies by an order of magnitude between the runs with the shortest and those with the longest durations (Fig. 8b). In particular, starting from a dwell time of ≥ 3 h,

the runs begin to achieve conditions close to the textural equilibrium, at which point kinetic processes (i.e. growth and nucleation) begin to slow down. In detail, as shown in Fig. 11a, Cpx crystallization is negligible after 15 min for the two samples with $\Delta T_{eff} \sim 100$ °C but continues for up to 3 h for the two samples with $\Delta T_{eff} \sim 50$ °C. Concerning the sizes of Cpx, instead, for all considered undercoolings, they show a general increase increasing the dwell time only up to 6 h runs (Fig. 8a), remaining approximately constant for longer experimental times. All that suggests that the G_L values determined for long-lasting (> 6 h) experiments are apparent and that, at this point, we are approaching conditions near to the textural equilibrium (Fig. 11; Arzilli et al. 2015). The influence of time on crystal growth rate thus appears to be strictly related to the equilibration time of the growing phases, as observed by previous studies (e.g. Couch 2003; Couch et al. 2003; Orlando et al. 2008; Arzilli et al. 2015). These authors, indeed, noted that the growth of some mineral phases, such as plagioclase and clinopyroxene, require different times to reach the equilibrium conditions. For instance, time has no resolvable influence on plagioclase at experimental durations longer than 1–2 h, a time which appears to be sufficient for the Plg-melt system to approach a near-equilibrium state (Couch 2003; Couch et al. 2003; Arzilli et al. 2015). Clinopyroxene may also require longer times (of the order of 20 h; Orlando et al. 2008).

Differences of clinopyroxene growth rate

There are several studies of clinopyroxene growth (e.g. Baker 2008; Burkhard 2002, 2005; Orlando et al. 2008), although they are completely absent for high-pressure conditions (> 0.5 GPa). There is, though a difference between the pressure values of our study and those available in literature (e.g. Baker 2008; Burkhard 2002, 2005; Orlando et al. 2008; Oze and Winter 2005; Pontesilli et al. 2019; Shea and Hammer 2013; Simakin et al. 2003; Table S3). However, the Cpx growth rates (10^{-5}–10^{-9} cm·s^{-1}) appear to be comparable, since they show similar trends in the growth rate vs dwell time diagram (Fig. 12). In particular, our data combined with literature data outline three parallel trends. The first is an upper trend which includes *single-step* cooling and decompression experiments on a basaltic-andesite (dwell times of 12–48 h at 995–1025 °C and 65–150 MPa) as reported by Shea and Hammer (2013). It also includes the dynamic isothermal time-series experiments on a trachybasaltic composition (dwell times of 0.5–24 h at 1100 °C and 400 MPa) reported by Pontesilli et al. (2019), and is characterized by high growth rates. The second is a low end-member trend that includes the CSD analyses performed by Burkhard (2002) on re-heated Hawaiian basalts (crystal residence times of ~ 0.01–7 h) and by Oze and Winter (2005) on natural basalts (crystal residence times of ~ 0.04–9 h). It also includes the static experiments of Burkhard (2005) on re-

Fig. 10 CSD relation between the natural logarithm of the population density of crystals (ln(L)) and the crystal length (L) for the APR16-C1A (**a**), APR16-C1B (**b**), APR16-C2A (**c**) and APR16-C2B (**d**) subseries
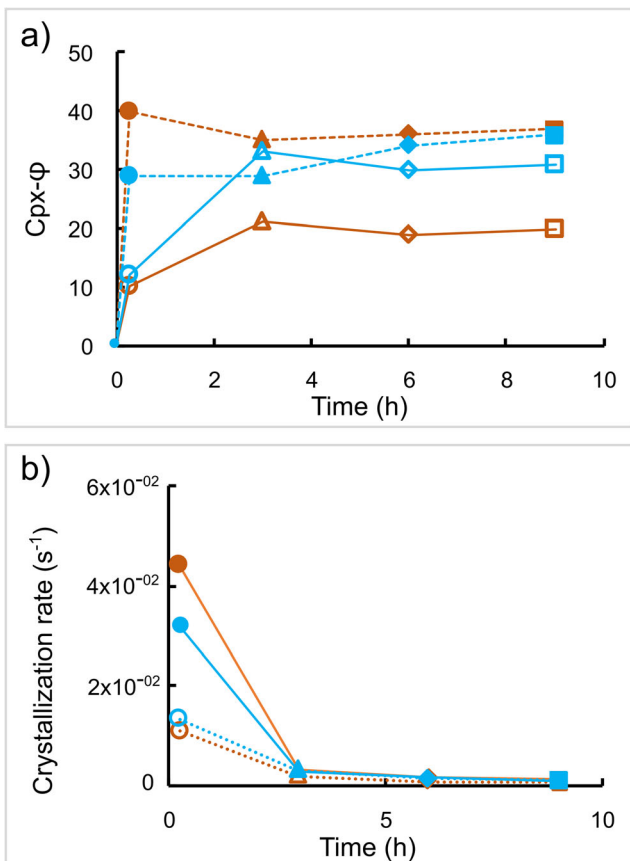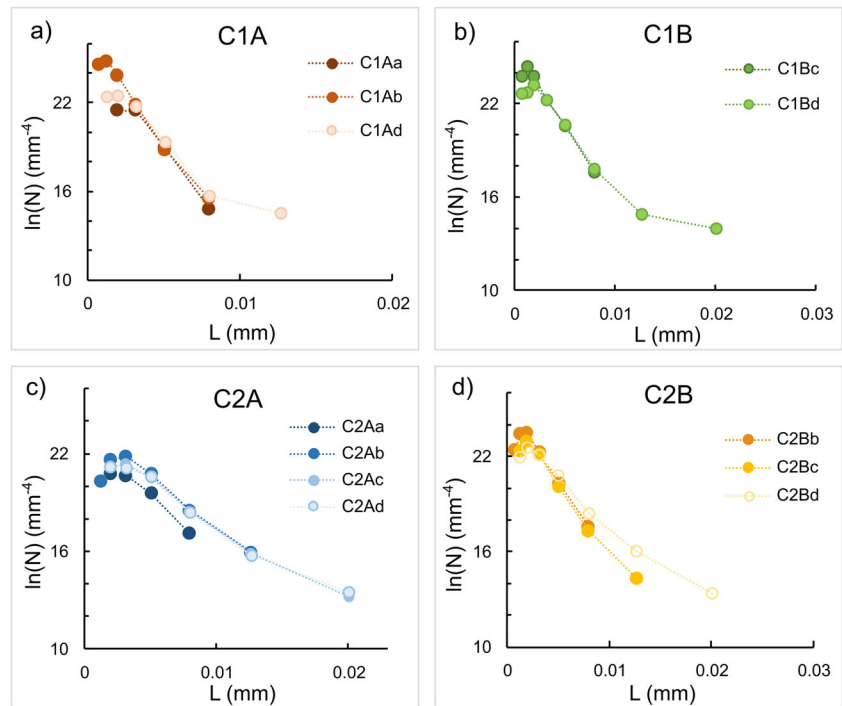

Fig. 11 Relation between **a** crystal fraction (Cpx-Φ) and time, and **b** crystallization rate and time. Symbols are as in Fig. 7

heated anhydrous basaltic glasses (dwell times of 22–576 h at 930–990 °C and 1 atm) and is characterized by low growth rate values. The third is a *middle trend* which includes our static experiments on the APR16 alkaline basalt and the experiments (dwell times of 3–40 h at 1170 °C and 1 atm) on a K-trachybasalt from Mt. Etna by Orlando et al. (2008). It is characterized by growth rate values between the two end-members. All of the above experiments were performed at different temperature conditions and H_2O contents (Table S4 in Online Resource 2), which are two key factors controlling the viscosity of magmas (e.g. Pinkerton and Stevenson 1992; Dingwell et al. 1993; Giordano et al. 2004). Notably, variations in melt viscosity deeply affect the kinetics of the crystallization process and then the value of G_L (Orlando et al. 2008; Vona and Romano 2013). Therefore, differences in melt viscosity appear to be the main factor in explaining the differences between the three trends observed in Fig. 12. For example, the runs of Shea and Hammer (2013) that fall in the upper trend (Fig. 12) were performed under saturation conditions. Hence, the high amount of water, reducing the viscosity and increasing element diffusivity in the melt, explains high growth rate values in respect to the runs that are undersaturated. Regarding the runs of the middle and the lower trends (Fig. 12), instead, the different growth rate values can be explained by taking into account the effect of chemical composition and temperature on the viscosity. The runs of the lower trend, indeed, were performed using a tholeiitic basalt as starting material. This is characterized by higher SiO_2 and lower Σ_{alkali} contents than the APR16-basalt of this study and the Mt. Etna trachybasalt of Orlando et al. (2008), making
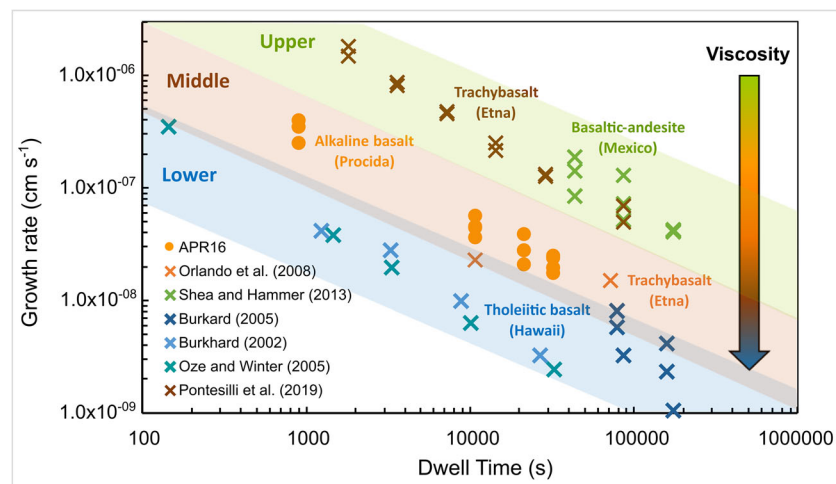
Fig. 12 Relation between crystal growth rate (G_L) and experimental duration (t) for this and previous studies on clinopyroxenes. Literature experimental data are from Burkhard (2002, 2005), Orlando et al. (2008), Oze and Winter (2005), Pontesilli et al. (2019) and Shea and Hammer (2013). The coloured fields represent: the upper trend in green, the middle trend in dark orange and the lower trend in light blue. Coloured fields correspond to different viscosity values (see Fig. S6 in Online Resource 1) that tend to increase from the upper to the lower trend, as shown by the coloured arrow on the right. The runs of Pontesilli et al. (2019), which should fall in the middle trend based on viscosity, fall instead in the upper one due to the higher undercooling and cooling rate

the tholeiitic melts of the lower trend more viscous than the alkaline ones of the middle trend (see below and Fig. S6 of Online Resource 1). This, consequently, determines the low growth rate values observed for such tholeiitic basaltic composition ($\sim 10^{-9}$ cm·s^{-1}), with respect to the G_L values ($\sim 10^{-8}$ cm·s^{-1}) obtained for the alkaline basalts of the middle trend (Fig. 12). Furthermore, the runs of the lower trend were carried out at lower temperatures (~ 900 °C) with respect to those of the middle trend (~ 1100–1250 °C). The high temperature, as well as the water content, will affect the crystal growth rate due to its depolymerizing effect, reducing viscosity and increasing element diffusivity in the melt (Ni et al. 2015).

To verify this hypothesis, we calculated the viscosity of all compositions reported in Fig. 12 at atmospheric pressure using the EXCEL® spreadsheet of Giordano et al. (2008). As seen in Fig. S6 in Online Resource 1, at the temperatures considered here (900–1200 °C), the samples have viscosity values that confirm our inference, since they match the distribution observed for the growth rates in the diagram of Fig. 12. However, the growth rates calculated by Pontesilli et al. (2019) for a trachybasaltic composition (10^{-6}–10^{-8} cm·s^{-1}) show values higher than those of the middle trend defined here in Fig. 12. We expect them to fall in this trend since they have a composition very close to the K-trachybasalt of Orlando et al. (2008) which is that plotted here. For this case viscosity cannot explain the different growth rate values between these two trachybasalts, since they show the same viscosity variation trend with temperature (Fig. S6 in Online Resource 1). Instead, we suggest that the difference in G_L is a function of the undercooling and the cooling rate (e.g. Lesher et al. 1999; Conte et al. 2006; Arzilli et al. 2015).

The experiments performed by Pontesilli et al. (2019), indeed, are characterized by a cooling rate of 80 °C/min and higher degrees of undercooling (80–120 °C) with respect to the static low undercooling ($\Delta T = 20$ °C) experiments of Orlando et al. (2008).

Considering, also, the influence of water content on crystal growth rate, due to its depolymerizing effect that reduces viscosity and increases element diffusivity in the melt (Hess and Dingwell 1996; Ni et al. 2015), in our experiments the calculated growth rates at different water contents remain in the same (order of magnitude) field (Fig. 13). In particular, we note that growth rates of runs with H$_2$O$_f$ (i.e. water dissolved in the melt) between 2 and 4 wt.% are slightly higher than those with H$_2$O$_f$ < 2 wt.%, and similar to those observed by
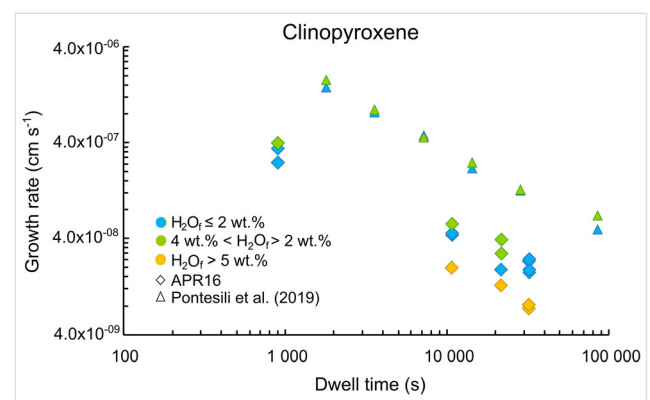

Fig. 13 Relation between Cpx growth rate (G_L) and water content dissolved in the melt (H$_2$O$_f$). Diamonds represent APR16 runs while triangles are the results of Pontesilli et al. (2019). Colours indicate different amounts of water content dissolved in the melt: H$_2$O$_f \leq 2$ wt.% in light blue, 4 wt.% < H$_2$O$_f$ > 2 wt.% in green, H$_2$O$_f$ > 5 wt.% in yellow

Pontesilli et al. (2019). The very minor influence of water on crystal growth rate, and consequently on viscosity of our results, and those of Pontesilli et al. (2019), is probably due to the composition used in the experiments; being alkaline in both cases. Alkaline magmas are more depolymerized than calc-alkaline compositions, due to the presence of alkalis that act as "modifier networks" (Hess et al. 1995). This difference has been noted in the literature, where the model accounting for non-Arrhenian variation of viscosity in calc-alkaline magmas has been proved to not apply to alkaline magmas (Giordano et al. 2006).

Moreover, growth rates calculated in runs with high-water contents in the melt (> 5 wt.%) are lower than those obtained for runs with lower water contents (1–3 wt.%). As observed by Bonechi et al. (2019), this is probably due to the dominance on crystallization of the hydrous phase, amphibole, which grows at the expense of Cpx that, indeed, never exceeds a size of ~ 10 μm in our experiments (Fig. 8a).

Magma refilling of the deep reservoir of the Campi Flegrei Volcanic District

Measurements of CSD, when combined with experimental growth rate data, can provide useful information to better constrain the time of magma crystallization (Cashman and Marsh 1988; Marsh 1988; Piochi et al. 2005b; Armienti et al. 2007; Brugger and Hammer 2010b; Arzilli et al. 2016). To date, there is limited kinetic data (crystal growth rate) on alkaline products and most of them concern feldspar minerals (e.g. Orlando et al. 2008; Agostini et al. 2013; Arzilli et al. 2015). Here we focused on Cpx growth rate, since (i) as demonstrated by Perinelli et al. (2019), clinopyroxene is the liquidus phase of the APR16 composition at high pressure (0.8 GPa), and (ii) thermobarometric estimates obtained from natural less-evolved samples of CFVD indicate an initial stage of clinopyroxene crystallization near the Moho (~ 25 km depth; Di Stefano et al. 2011). Moreover, Cpx growth rate data combined with thermobarometric data provide an estimate of deep-level ascent rate for CFVD primitive magmas (Armienti et al. 2013). We assume that a deep episode of magmatic crystallization takes place at low undercooling, a condition that produces slow crystal growth rates. This condition has been verified, here, by CSD investigations for clinopyroxene growth of natural samples. Cpx-CSDs were measured for two K-basaltic scoria clasts (SCE and SOG samples) collected in the deposit of the Solchiaro tuff ring (of Procida island). Both SCE and SOG have chemical compositions very close to that of APR16 sample (Table 1, Table S5 in Online Resource 2 and Online Resource 3). Note that, parameters used for the CSD analysis of natural samples were the same as those used for the experimental runs applied here.

CSD results for these two scoria clasts show an upward curvature (Fig. 14). This indicates the possible involvement
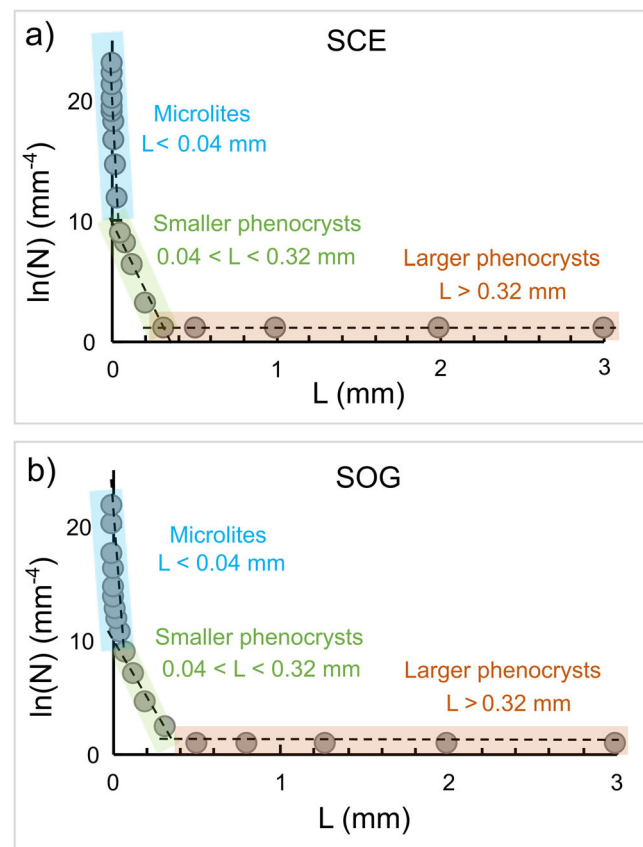

Fig. 14 Relation between population density (ln(N)) and length (L) of clinopyroxenes for SCE (**a**) and SOG (**b**) natural samples. Coloured rectangles indicate three different Cpx populations: in orange larger phenocrysts (L > 0.32 mm); in green smaller phenocrysts (0.04 < L < 0.32 mm); in light blue microlites (L < 0.04 mm)

of a number of processes, including changes in the magma cooling rate, crystal aggregation, magma mixing, or textural coarsening, during the crystallization history of these samples (Armienti et al. 1994; Higgins 1998, 2002; Higgins and Roberge 2003; Marsh 1998; Zieg and Marsh 2002). We recognize three populations of clinopyroxenes, each of which has an almost linear distribution (Fig. 14). The first population is of larger phenocrysts with size > 0.32 mm that can be interpreted as early-formed phenocrysts. The second is of smaller phenocrysts with sizes between 0.04 and 0.32 mm. The third involves microlites with L < 0.04 mm. The portion of the CSD plot relative to the larger phenocrysts shows that, on the basis of their composition and thermobarometric data (see Online Resource 3), they formed during a crystallization stage at a deep (20–25 km) level. This is apparent from an almost horizontal slope and a low intercept, which suggests that these crystals formed at low and almost constant undercooling and growth rates (Armienti et al. 1994). Using the growth rate value obtained here of $2.2 \cdot 10^{-8}$ cm·s^{-1} (i.e. the average of G_L values that on the basis of $K_D(Fe-Mg)^{Cpx-liq}$ fall in the field representing equilibrium conditions; Fig. S7 in Online Resource 1), it is possible to evaluate the minimum

growth time. Using this value, a minimum residence time of the largest SCE and SOG clinopyroxenes can be obtained (Cashman and Marsh 1988; Armienti et al. 1994). This value is estimated as ~ 5 months for a Cpx growth of ~ 3 mm. Moreover, the ascent rate of primitive CFVD magmas can be assessed by combining data on Cpx growth rate with thermobarometric data of natural clinopyroxenes (Armienti et al. 2013). The range of temperatures and pressures of crystallization estimated for the larger population of clinopyroxenes obtained here are 1141–1178 °C and 0.7–0.9 GPa (which converts to a 20–25 km depth assuming an average crustal density of 2.8 g·cm^{-3}). According to the approach of Armienti et al. (2013), for a ΔT of 37 °C (ΔT = 1178–1141 °C), a ΔL of ~ 0.3 cm (based on the magnitude of deep growth of clinopyroxene from CSD analyses; Fig. 14) and a growth rate of 2.2·10^{-8} cm·s^{-1}, as estimated by our experiments, the cooling rate during the ascent of CFVD K-basaltic magmas can be estimated to be 0.3·10^{-5} °C/s. This value, combined with the dP/dT from thermobarometry (see Online Resource 3), provides a deep-level ascent velocity of ~ 0.5·10^{-4} m·s^{-1}, which is comparable with the average magma transport rate of 3.6·10^{-4} m·s^{-1} estimated for Mt. Etna for depth > 6 km (Armienti et al. 2013). Nevertheless, the olivine/clinopyroxene ratio (~ 1) of the SCE and SOG scoriae indicates, according to the experimental phase relations at 0.2–0.8 GPa (Granati 2016), that the most primitive magmas of CFVD pond at relatively shallow levels before eruption. This is confirmed by barometric estimates based on the smaller phenocrysts, whose crystallization onset occurred at 0.3–0.5 GPa (8–14 km depth; see Online Resource 3). Consequently, the calculated residence time of the larger Cpx population (i.e. 5 months at least) multiplied by the magma volume erupted from the CFVD tuff ring (0.1–1 km^3; Mastrolorenzo et al. 2017) could represent the minimum recharge rate of the large magmatic reservoir, whose top has been located in the CFVD at a depth of about 8 km (e.g. Rapolla et al. 1989; Cecchetti et al. 2001; Auger et al. 2001; Zollo et al. 2008; Esposito et al. 2011; Pappalardo and Mastrolorenzo 2012; Fanara et al. 2015; Fedi et al. 2018).

Conclusions

Through this work, we have improved knowledge of crystallization kinetics of clinopyroxene in alkaline basaltic melts, providing new crystal growth rate data under high-pressure conditions. At the investigated conditions, clinopyroxene growth rate (G_L) is strongly affected by time, with values that vary from 10^{-7} to 10^{-8} cm·s^{-1} from the shortest (0.25 h) to the longer-lasting (6–9 h) experiments. By comparing our clinopyroxene growth rate data with those available in the literature, we observe that viscosity, and the parameters that control it (temperature, water content and chemical composition), undercooling and cooling rate are the factors that most affect crystal growth rate. This is a result of their control over element diffusivity in the melt. On the other hand, pressure appears to have no influence on crystal growth rate. The experimental Cpx growth rate combined with data from CSD and thermobarometry of CFVD clinopyroxenes suggests that recharge by primitive magmas in the deep CFVD reservoirs occurs with a relatively high ascent rate (~ 0.5·10^{-4} m·s^{-1}).

References

Abramoff MD, Magalhães PJ, Ram SJ (2004) Image processing with ImageJ. Biophoton Int 11:36–42

Agostini C, Fortunati A, Arzilli F et al (2013) Kinetics of crystal evolution as a probe to magmatism at Stromboli (Aeolian Archipelago, Italy). Geochim Cosmochim Acta 110:135–151. https://doi.org/10.1016/j.gca.2013.02.027

Armienti P, Pareschi MT, Innocenti F, Pompilio M (1994) Effects of magma storage and ascent on the kinetics of crystal growth—the case of the 1991-93 Mt. Etna eruption. Contrib Mineral Petrol 115:402–414. https://doi.org/10.1007/BF00320974

Armienti P, Tonarini S, Orazio MD (2007) Mount Etna pyroxene as tracer of petrogenetic processes and dynamics of the feeding system. Geol Soc Am Spec Pap:265–276. https://doi.org/10.1130/2007.2418(13)

Armienti P, Perinelli C, Putirka KD (2013) A new model to estimate deep-level magma ascent rates, with applications to Mt. Etna (Sicily, Italy). J Petrol 54:795–813. https://doi.org/10.1093/petrology/egs085

Arzilli F, Carroll MR (2013) Crystallization kinetics of alkali feldspars in cooling and decompression-induced crystallization experiments in trachytic melt. Contrib Mineral Petrol 166:1011–1027. https://doi.org/10.1007/s00410-013-0906-1

Arzilli F, Agostini C, Landi P, Fortunati A, Mancini L, Carroll MR (2015) Plagioclase nucleation and growth kinetics in a hydrous basaltic melt by decompression experiments. Contrib Mineral Petrol 170:55–16. https://doi.org/10.1007/s00410-015-1205-9

Arzilli F, Piochi M, Mormone A, Agostini C, Carroll MR (2016) Constraining pre-eruptive magma conditions and unrest timescales during the Monte Nuovo eruption (1538 AD; Campi Flegrei, Southern Italy): integrating textural and CSD results from experimental and natural trachy-phonolites. Bull Volcanol 78:72–20. https://doi.org/10.1007/s00445-016-1062-z

Asimow P, Ghiorso MS (1998) Algorithmic modifications extending MELTS to calculate subsolidus phase relations. Am Mineral 83:1127–1132

Auger E, Gasparini P, Virieux J, Zollo A (2001) Seismic evidence of an extended magmatic sill under Mt. Vesuvius. Science 294:1510–1512. https://doi.org/10.1126/science.1064893

Baker DR (2008) The fidelity of melt inclusions as records of melt composition. Contrib Mineral Petrol 156:377–395. https://doi.org/10.1007/s00410-008-0291-3

Bonechi B, Perinelli C, Gaeta M et al (2017) Experimental constraints on amphibole stability in primitive alkaline and calc-alkaline magmas. Period Mineral 86:231–245. https://doi.org/10.2451/2017PM735

Bonechi B, Perinelli C, Gaeta M et al (2019) Amphibole growth from a primitive alkaline basalt at 0.8 GPa: time-dependent compositional evolution, growth rate and competition with clinopyroxene. Lithos. https://doi.org/10.1016/j.lithos.2019.105272

Brugger CR, Hammer JE (2010a) Crystal size distribution analysis of plagioclase in experimentally decompressed hydrous rhyodacite magma. Earth Planet Sci Lett. https://doi.org/10.1016/j.epsl.2010.09.046

Brugger CR, Hammer JE (2010b) Crystallization kinetics in continuous decompression experiments: implications for interpreting natural magma ascent processes. J Petrol 51:1941–1965. https://doi.org/10.1093/petrology/egq044

Burkhard DJ (2002) Kinetics of crystallization: example of micro-crystallization in basalt lava. Contrib Mineral Petrol 142:724–737. https://doi.org/10.1007/s00410-001-0321-x

Burkhard DJM (2005) Nucleation and growth rates of pyroxene, plagioclase, and Fe-Ti oxides in basalt under atmospheric conditions. Eur J Mineral 17:675–686. https://doi.org/10.1127/0935-1221/2005/0017-0675

Cashman KV (1993) Relationship between plagioclase crystallization and cooling rate in basaltic melts. Contrib Mineral Petrol 113:126–142

Cashman CV, Marsh BD (1988) Crystal size distribution (CSD) in rocks and the kinetics and dynamics of crystallisation. Contrib Mineral Petrol 99:292–305. https://doi.org/10.1007/BF00371933

Cecchetti A, Marianelli P, Sbrana A (2001) Prime evidenze della esistenza di un sistema di cristallizzazione profondo ai Campi Flegrei. Atti Soc Tosc Sci Nat Mem:1–7

Chiarabba C, De Gori P, Speranza F (2008) The southern Tyrrhenian subduction zone: deep geometry, magmatism and Plio-Pleistocene evolution. Earth Planet Sci Lett 268:408–423. https://doi.org/10.1016/j.epsl.2008.01.036

Clarke AB, Stephens S, Teasdale R et al (2007) Petrologic constraints on the decompression history of magma prior to Vulcanian explosions at the Soufrière Hills volcano, Montserrat. J Volcanol Geotherm Res 161:261–274. https://doi.org/10.1016/j.jvolgeores.2006.11.007

Conte AM, Perinelli C, Trigila R (2006) Cooling kinetics experiments on different Stromboli lavas: effects on crystal morphologies and phases composition. J Volcanol Geotherm Res 155:179–200. https://doi.org/10.1016/j.jvolgeores.2006.03.025

Conte AM, Dolfi D, Gaeta M et al (2009) Experimental constraints on evolution of leucite-basanite magma at 1 and 10-4 GPa: implications for parental compositions of Roman high-potassium magmas. Eur J Mineral 21:763–782. https://doi.org/10.1127/0935-1221/2009/0021-1934

Couch S (2003) Experimental investigation of crystallization kinetics in a haplogranite system. Am Mineral 88:1471–1485

Couch S, Sparks RSJ, Carroll MR (2003) The kinetics of degassing-induced crystallization at Soufriere Hills Volcano, Montserrat. J Petrol 44:1477–1502. https://doi.org/10.1093/petrology/44.8.1477

D'Antonio M, Civetta L, Di Girolamo P (1999) Mantle source heterogeneity in the Campanian region (South Italy) as inferred from geochemical and isotopic features of mafic volcanic rocks with shoshonitic affinity. Mineral Petrol 67:163–192. https://doi.org/10.1007/BF01161520

De Astis G, Pappalardo L, Piochi M (2004) Procida volcanic history: new insights into the evolution of the Phlegraean Volcanic District (Campania region, Italy). Bull Volcanol 66:622–641. https://doi.org/10.1007/s00445-004-0345-y

Devine JD, Gardner JE, Brack HP et al (1995) Comparison of microanalytical methods for estimating H2O contents of silicic volcanic glasses. Am Mineral 80:319–328. https://doi.org/10.2138/am-1995-3-413

Di Stefano R, Chiarabba C, Lucente F, Amato A (1999) Crustal and uppermost mantle structure in Italy. Geophys J Int 139:438–498

Di Stefano R, Bianchi I, Ciaccio MG et al (2011) Three-dimensional Moho topography in Italy: new constraints from receiver functions and controlled source seismology. Geochem Geophys Geosyst 12:1–15. https://doi.org/10.1029/2011GC003649

Dingwell DB, Bagdassarov NS, Bussod GY, Webb SL (1993) Magma rheology. In: Luth RH (ed) Short course handbook on experiments at high pressure and applications to Earth's mantle, vol. 21

Dowty E, Keil K, Prinz M (1974) Lunar pyroxene-phyric basalts: crystallization under supercooled conditions. J Petrol 15:419–453. https://doi.org/10.1093/petrology/15.3.419

Esposito R, Bodnar RJ, Danyushevsky LV et al (2011) Volatile evolution of magma associated with the solchiaro eruption in the Phlegrean Volcanic District (Italy). J Petrol 52:2431–2460. https://doi.org/10.1093/petrology/egr051

Fanara S, Botcharnikov RE, Palladino DM et al (2015) Volatiles in magmas related to the Campanian ignimbrite eruption: experiments vs. natural findings. Am Mineral 100:2284–2297. https://doi.org/10.2138/am-2015-5033

Faure F, Schiano P (2005) Experimental investigation of equilibration conditions during forsterite growth and melt inclusion formation. Earth Planet Sci Lett 236:882–898. https://doi.org/10.1016/j.epsl.2005.04.050

Faure F, Trolliard G, Nicollet C, Montel JM (2003) A developmental model of olivine morphology as a function of the cooling rate and the degree of undercooling. Contrib Mineral Petrol 145:251–263. https://doi.org/10.1007/s00410-003-0449-y

Fedi M, Cella F, D'Antonio M, Florio G, Paoletti V, Morra V (2018) Gravity modeling finds a large magma body in the deep crust below the Gulf of Naples, Italy. Sci Rep 8:1–19. https://doi.org/10.1038/s41598-018-26346-z

Ghiorso MS, Sack RO (1995) Chemical mass transfer in magmatic processes IV. A revised and internally consistent thermodynamic model for the interpolation and extrapolation of liquid-solid equilibria in magmatic systems at elevated temperatures and pressures. Contrib Mineral Petrol. https://doi.org/10.1007/BF00307281

Giordano D, Romano C, Papale P, Dingwell DB (2004) The viscosity of trachytes, and comparison with basalts, phonolites, and rhyolites. Chem Geol 213:49–61. https://doi.org/10.1016/j.chemgeo.2004.08.032

Giordano D, Mangiacapra A, Potuzak M et al (2006) An expanded non-Arrhenian model for silicate melt viscosity: a treatment for metaluminous, peraluminous and peralkaline liquids. Chem Geol 229:42–56. https://doi.org/10.1016/j.chemgeo.2006.01.007

Giordano D, Russell JK, Dingwell DB (2008) Viscosity of magmatic liquids: a model. Earth Planet Sci Lett 271:123–134. https://doi.org/10.1016/j.epsl.2008.03.038

Granati SF (2016) The architecture of the magmatic feeding system of the Campi Flegrei Volcanic District: constraints from experimental petrology. Sapienza University of Rome, Rome

Grove TL, Raudsepp M (1978) Effects of kinetics on the crystallization of quartz normative basalt 15597-an experimental study. Proc Lunar Planet Sci Conf 9:585–599

Grove TL, Walker D (1977) Cooling histories of Apollo 15 quartz-normative basalts. Proc Lunar Planet Sci Conf 8:1501–1520

Hammer JE (2006) Influence of fO2 and cooling rate on the kinetics and energetics of Fe-rich basalt crystallization. Earth Planet Sci Lett 248:618–637. https://doi.org/10.1016/j.epsl.2006.04.022

Hammer JE (2008) Experimental studies of the kinetics and energetics of magma crystallization. In: Putirka KD, Tepley III FJ (eds) Minerals, inclusions and volcanic processes. Rev Mineral Geochemistry, pp 9–59

Hammer JE, Rutherford MJ (2002) An experimental study of the kinetics of decompression-induced crystallization in silicic melt. J Geophys Res 107:2021. https://doi.org/10.1029/2001JB000281

Hammer JE, Cashman KV, Voight B (2000) Magmatic processes revealed by textural and compositional trends in Merapi dome lavas. J Volcanol Geotherm Res 100:165–192. https://doi.org/10.1016/S0377-0273(00)00136-0

Helz RT, Wright T (1992) Differentiation and magma mixing on Kilauea's east rift zone A further look at the eruptions of 1955 and 1960. Part I. The late 1955 lavas. Bull Volcanol 54:361–384

Hess K, Dingwell DD (1996) Viscosities of hydrous leucogranitic melts: a non-Arrhenian on the nature and efficiency of magmatic processes. As pendence (H20 concentration in weight percent) for each. Am Mineral 81:1297–1300

Hess KU, Dingwell DB, Webb SL (1995) The influence of excess alkalis on the viscosity of a haplogranitic melt. Am Mineral 80:297–304. https://doi.org/10.2138/am-1996-9-1014

Higgins MD (1994) Numerical modeling of crystal shapes in thin section: estimation of crystal habit and true size. Am Mineral 79:113–119

Higgins MD (1998) Origin of anorthosite by textural coarsening: quantitative measurements of a natural sequence of textural development. J Petrol 39:1307–1323. https://doi.org/10.1093/petroj/39.7.1307

Higgins DM (2000) Measurement of crystal size distributions. Am Mineral 85:1105–1116

Higgins MD (2002) Closure in crystal size distributions (CSD), verification of CSD calculations, and the significance of CSD fans. Am Mineral 87:1242–1243. https://doi.org/10.2138/am-2002-0118

Higgins MD, Roberge J (2003) Crystal size distribution of plagioclase and amphibole from Soufriere Hills Volcano, Montserrat: evidence for dynamic crystallization-textural coarsening cycles. J Petrol 44: 1401–1411. https://doi.org/10.1093/petrology/44.8.1401

Iezzi G, Mollo S, Torresi G et al (2011) Experimental solidification of an andesitic melt by cooling. Chem Geol 283:261–273. https://doi.org/10.1016/j.chemgeo.2011.01.024

Johannes W, Bell PM, Mao HK et al (1971) An interlaboratory comparison of piston-cylinder pressure calibration using the albite-breakdown reaction. Contrib Mineral Petrol 32:24–38. https://doi.org/10.1007/BF00372231

Kirkpatrick RJ, Kuo L, Melchior J (1981) Crystal growth in incongruently-melting compositions: programmed cooling experiments with diopside. Am Mineral 66:223–241

Kress VC, Carmichael ISE (1991) The compressibility of silicate liquids containing Fe2O3 and the effect of composition, temperature, oxygen fugacity and pressure on their redox states. Contrib Mineral Petrol 108:82–92. https://doi.org/10.1007/BF00307328

Lentz RCF, Mcsween HY (2000) Crystallization of the basaltic shergottites: insights from crystal size distribution (CSD) analysis of pyroxenes. Meteorit Planet Sci 35:919–927. https://doi.org/10.1111/j.1945-5100.2000.tb01481.x

Lesher CE, Cashman KV, Mayfield JD (1999) Kinetic controls on crystallization of Tertiary North Atlantic basalt and implications for the emplacement and cooling history of lava at site 989, Southeast Greenland Rifted Margn 1. In: Proceedings of the Ocean Drilling Program, Scientific Results. pp 135–148

Lofgren GE (1974) An experimental study of plagioclase crystal morphology; isothermal crystallization. Am J Sci 274:243–273

Lofgren GE (1980) Experimental studies on the dynamic crystallization of silicate melts

Lofgren GE (1983) Effect of heterogeneous nucleation on basaltic textures: a dynamic crystallization study. J Petrol 24:229–255. https://doi.org/10.1093/petrology/24.3.229

Mangan MT (1990) Crystal size distribution systematics and the determination of magma storage times: the 1959 eruption of Kilauea volcano, Hawaii. J Volcanol Geotherm Res 44:295–302. https://doi.org/10.1016/0377-0273(90)90023-9

Marsh BD (1988) Crystal size distribution (CSD) in rocks and the kinetics and dynamics of crystallization. Contrib Mineral Petrol 99:277–291. https://doi.org/10.1007/BF00375362

Marsh BD (1998) On the interpretation of crystal size distributions in magmatic systems. J Petrol 39:553–599. https://doi.org/10.1093/petroj/39.4.553

Mastrolorenzo G, Palladino DM, Pappalardo L, Rossano S (2017) Probabilistic-numerical assessment of pyroclastic current hazard at Campi Flegrei and Naples city: multi-VEI scenarios as a tool for "full-scale" risk management. PLoS One 12:1–28. https://doi.org/10.1371/journal.pone.0185756

Melnik O, Sparks RSJ (2005) Control on conduit magma flows dynamics during lava dome building eruptions. J Geophys Res 110:B02209

Moretti R, Arienzo I, Orsi G et al (2013) The deep plumbing systemof ischia: a physico-chemicalwindowon the fluid-saturated and CO2-sustained neapolitanvolcanism (southern Italy). J Petrol 54:951–984. https://doi.org/10.1093/petrology/egt002

Morimoto N, Fabries J, Ferguson AK et al (1998) Nomenclature of pyroxenes subcommittee. Am Mineral 73:1123–1133

Mormone A, Piochi M, Bellatreccia F et al (2011) A CO2-rich magma source beneath the Phlegraean Volcanic District (Southern Italy): evidence from a melt inclusion study. Chem Geol 287:66–80. https://doi.org/10.1016/J.CHEMGEO.2011.05.019

Ni H, Keppler H, Walte N, Schiavi F, Chen Y, Masotta M, Li Z (2014) In situ observation of crystal growth in a basalt melt and the development of crystal size distribution in igneous rocks. Contrib Mineral Petrol 167:1–13. https://doi.org/10.1007/s00410-014-1003-9

Ni H, Hui H, Steinle-Neumann G (2015) Transport properties of silicate melts. Rev Geophys 53:715–744. https://doi.org/10.1029/88EO01108

Orlando A, D'Orazio M, Armienti P, Borrini D (2008) Experimental determination of plagioclase and clinopyroxene crystal growth rates in an anhydrous trachybasalt from Mt Etna (Italy). Eur J Mineral 20: 653–664. https://doi.org/10.1127/0935-1221/2008/0020-1841

Oze C, Winter JD (2005) The occurrence, vesiculation, and solidification of dense blue glassy pahoehoe. J Volcanol Geotherm Res 142:285–301. https://doi.org/10.1016/j.jvolgeores.2004.11.008

Pan Y, Batiza R (2002) Mid-ocean ridge magma chamber processes: constraints from olivine zonation in lavas from the East Pacific Rise at 9°30′N and 10°30′N. J Geophys Res Solid Earth 107:ECV 9-1–ECV 9-13. https://doi.org/10.1029/2001jb000435

Pappalardo L, Mastrolorenzo G (2012) Rapid differentiation in a sill-like magma reservoir: a case study from the campi flegrei caldera. Sci Rep 2:712. https://doi.org/10.1038/srep00712

Perinelli C, Mollo S, Gaeta M et al (2018) Impulsive supply of volatile-rich magmas in the shallow plumbing system of Mt. Etna Volcano. Minerals 8:482. https://doi.org/10.3390/min8110482

Perinelli C, Gaeta M, Bonechi B et al (2019) Effect of water on the phase relations of primitive K-basalts: implications for high-pressure differentiation in the Phlegraean Volcanic District magmatic system. Lithos 342–343:530–541. https://doi.org/10.1016/j.lithos.2019.05.032

Philpotts A, Ague J (2009) Principles of igneous and metamorphic petrology, Cambridge

Pinkerton H, Stevenson RJ (1992) Methods of determining the rheological properties of magmas at sub-liquidus temperatures. J Volcanol Geotherm Res 53:47–66. https://doi.org/10.1016/0377-0273(92)90073-M

Piochi M, Bruno PP, De Astis G (2005a) Relative roles of rifting tectonics and magma ascent processes: inferences from geophysical, structural, volcanological, and geochemical data for the Neapolitan volcanic region (southern Italy). Geochem Geophys Geosyst 6. https://doi.org/10.1029/2004GC000885

Piochi M, Mastrolorenzo G, Pappalardo L (2005b) Magma ascent and eruptive processes from textural and compositional features of Monte Nuovo pyroclastic products, Campi Flegrei, Italy. Bull Volcanol 67:663–678. https://doi.org/10.1007/s00445-005-0410-1

Polacci M, Arzilli F, La Spina G et al (2018) Crystallisation in basaltic magmas revealed via in situ 4D synchrotron X-ray

microtomography. Sci Rep 8:1–13. https://doi.org/10.1038/s41598-018-26644-6

Pontesilli A, Masotta M, Nazzari M et al (2019) Crystallization kinetics of clinopyroxene and titanomagnetite growing from a trachybasaltic melt: new insights from isothermal time-series experiments. Chem Geol 510:113–129. https://doi.org/10.1016/j.chemgeo.2019.02.015

Pouchou JL, Pichoir F (1991) Quantitative analysis of homogeneous or stratified microvolumes applying the model "PAP". In: Heinrich KFJ, Newbury DE (eds) Reserche Aereospatiale, Electron p. Plenum Press, New York, pp 31–75

Presnall DC, Dixon SA, Dixon JR et al (1978) Liquidus phase relations on the join diopside-forsterite-anorthite from 1 atm to 20 kbar: their bearing on the generation and crystallization of basaltic magma. Contrib Mineral Petrol 66:203–220. https://doi.org/10.1007/BF00372159

Pupier E, Duchene S, Toplis MJ (2008) Experimental quantification of plagioclase crystal size distribution during cooling of a basaltic liquid. Contrib Mineral Petrol 155:555–570. https://doi.org/10.1007/s00410-007-0258-9

Putirka K (1999) Clinopyroxene + liquid equilibria to 100 kbar and 2450 K. Contrib Mineral Petrol 135:151–163. https://doi.org/10.1007/s004100050503

Putirka KD (2008) Thermometers and barometers for volcanic systems. In: Putirka KD, Tepley III FJ (eds) Minerals, inclusions and volcanic processes. Reviews in Mineralogy and Geochemistry, pp 61–120

Putirka KD, Mikaelian H, Ryerson F, Shaw H (2003) New clinopyroxene-liquid thermobarometers for mafic, evolved, and volatile-bearing lava compositions, with applications to lavas from Tibet and the Snake River Plain, Idaho. Am Mineral 88:1542–1554

Randolph AD, Larson MA (1971) Theory of particulate processes. Academic, New York

Rapolla A, Fedi M, Fiume MG (1989) Crustal structure of the Ischia-Phlegrean geothermal fields, near Naples, Italy, from gravity and aeromagnetic data. Geophys J Int 97:409–419. https://doi.org/10.1111/j.1365-246X.1989.tb00511.x

Schneider CA, Rasband WS, Eliceiri KW (2012) NIH image to ImageJ: 25 years of image analysis. Nat Methods 9:671–675. https://doi.org/10.1038/nmeth.2089

Shea T, Hammer JE (2013) Kinetics of cooling- and decompression-induced crystallization in hydrous mafic-intermediate magmas. J Volcanol Geotherm Res 260:127–145. https://doi.org/10.1016/j.jvolgeores.2013.04.018

Simakin AG, Salova TP, Armienti P (2003) Kinetics of clinopyroxene growth from a hydrous hawaiite melt. Geochem Int 41:1275–1285

Thornber CR (2001) Olivine-liquid relations of lava erupted by Kilauea volcano from 1994 to 1998: implications for shallow magmatic processes associated with the ongoing east-rift-zone eruption. Can Mineral 39:239–266. https://doi.org/10.2113/gscanmin.39.2.239

Toplis MJ (2005) The thermodynamics of iron and magnesium partitioning between olivine and liquid: criteria for assessing and predicting equilibrium in natural and experimental systems. Contrib Mineral Petrol 149:22–39. https://doi.org/10.1007/s00410-004-0629-4

Vona A, Romano C (2013) The effects of undercooling and deformation rates on the crystallization kinetics of Stromboli and Etna basalts. Contrib Mineral Petrol 166:491–509. https://doi.org/10.1007/s00410-013-0887-0

Walker D, Powell MA, Lofgren GE, Hays JF (1978) Dynamic crystallization of a eucrite basalt. In: Lunar and Planetary Science Conference Proceedings. pp 1369–1391

Weaver SL, Wallace PJ, Johnston AD (2013) Experimental constraints on the origins of primitive potassic lavas from the Trans-Mexican Volcanic Belt. Contrib Mineral Petrol 166:825–843. https://doi.org/10.1007/s00410-013-0921-2

Zieg MJ, Lofgren GE (2006) An experimental investigation of texture evolution during continuous cooling. J Volcanol Geotherm Res 154:74–88. https://doi.org/10.1016/j.jvolgeores.2005.09.020

Zieg MJ, Marsh BD (2002) Crystal size distributions and scaling laws in the quantification of igneous textures. J Petrol 43:85–101. https://doi.org/10.1093/petrology/43.1.85

Zollo A, Maercklin N, Vassallo M et al (2008) Seismic reflections reveal a massive melt layer feeding Campi Flegrei caldera. Geophys Res Lett 35:0–5. https://doi.org/10.1029/2008GL034242